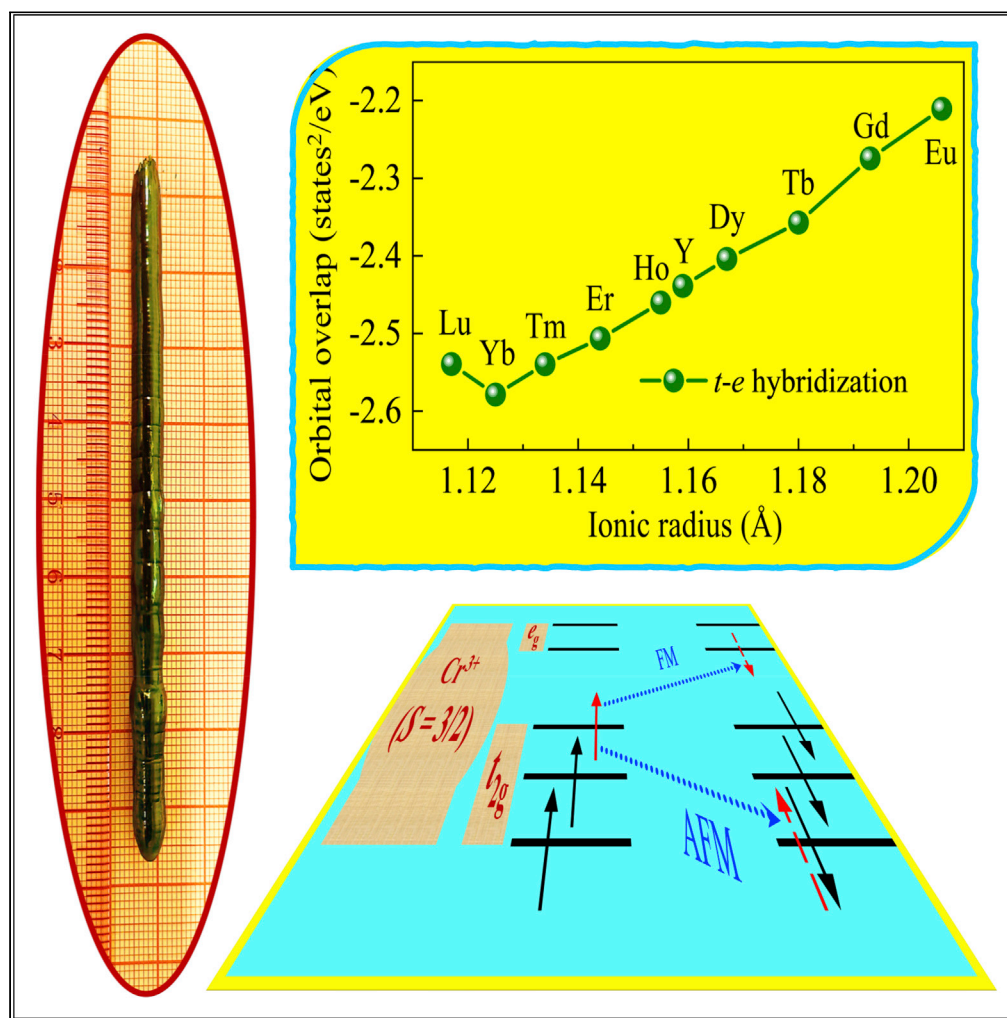**Article**

Crystal growth engineering and origin of the weak ferromagnetism in antiferromagnetic matrix of orthochromates from *t-e* orbital hybridization

Yinghao Zhu, Junchao Xia, Si Wu, ..., Jianding Yu, Ruiqin Zhang, Hai-Feng Li

yujianding@mail.sic.ac.cn (J.Y.)
aprqz@cityu.edu.hk (R.Z.)
haifengli@um.edu.mo (H.-F.L.)

Highlights

The lack of large and good-quality single crystals of orthochromates has been solved

Nature of the weak ferromagnetism in a main antiferromagnetic matrix has been revealed

t-e orbital hybridization is the microscopic origin

Relationship between microscopic and macroscopic properties has been correlated

Article

Crystal growth engineering and origin of the weak ferromagnetism in antiferromagnetic matrix of orthochromates from *t-e* orbital hybridization

Yinghao Zhu,[1,2,3,4,5] Junchao Xia,[1,4,5] Si Wu,[1,4,5] Kaitong Sun,[1] Yuewen Yang,[2] Yanling Zhao,[2] Hei Wun Kan,[2] Yang Zhang,[3] Ling Wang,[3] Hui Wang,[3] Jinghong Fang,[3] Chaoyue Wang,[3] Tong Wu,[3] Yun Shi,[3] Jianding Yu,[3,*] Ruiqin Zhang,[2,*] and Hai-Feng Li[1,6,*]

SUMMARY

We report a combined experimental and theoretical study on intriguing magnetic properties of quasiferroelectric orthochromates. Large single crystals of the family of $RECrO_3$ (RE = Y, Eu, Gd, Tb, Dy, Ho, Er, Tm, Yb, and Lu) compounds were successfully grown. Neutron Laue study indicates a good quality of the obtained single crystals. Applied magnetic field and temperature dependent magnetization measurements reveal their intrinsic magnetic properties, especially the antiferromagnetic (AFM) transition temperatures. Density functional theory studies of the electronic structures were carried out using the Perdew-Burke-Ernzerhof functional plus Hubbard U method. Crystallographic information and magnetism were theoretically optimized systematically. When RE^{3+} cations vary from Y^{3+} and Eu^{3+} to Lu^{3+} ions, the calculated $t-e$ orbital hybridization degree and Néel temperature behave similarly to the experimentally determined AFM transition temperature with variation in cationic radius. We found that the $t-e$ hybridization is anisotropic, causing a magnetic anisotropy of Cr^{3+} sublattices. This was evaluated with the nearest-neighbor J_1-J_2 model. Our research provides a picture of the electronic structures during the $t-e$ hybridization process while changing RE ions and sheds light on the nature of the weak ferromagnetism coexisting with predominated antiferromagnetism. The available large $RECrO_3$ single crystals build a platform for further studies of orthochromates.

INTRODUCTION

Multiferroic materials have received considerable attention because of their potential application in electric and magnetic devices (Fiebig et al., 2016; Huang et al., 2021; Hur et al., 2004; Jones et al., 2014; Spaldin and Ramesh, 2019). Within the materials, long-range orders such as ferroelectric and magnetic coexist and may interact strongly on each other, providing multi-tunable parameters for tailoring the macroscopic functionalities. There are significant challenges for a complete understanding of the microscopic mechanisms underlying their intriguing macroscopic properties.

Chromium-based perovskites have attracted considerable interest because of their intriguing magnetic and ferroelectric properties as well as potential technique applications. The set of chromium-based $RECrO_3$ (RE = rare earths) compounds was suggested to be another family of multiferroic materials, usually displaying ferroelectricity, weak ferromagnetism, and a wide application in fields of catalyst, thermistor, solid-oxide fuel cell, and nonvolatile memory devices (Figure 1) (Oliveira, 2017). The formation of Cr^{3+} magnetic orders has a strong effect on the ferroelectric property, i.e., there may be a magnetoelectric coupling effect (Oliveira et al., 2020; Rajeswaran et al., 2012). Chromium ions in $RECrO_3$ compounds hold a single-valence state, i.e., Cr^{3+} ($t_{2g}^3 e_g^0$), naturally discarding the e_g orbital ordering as well as its perturbation on the t_{2g} electrons. This results in a tightly localized electric environment, an ideal platform for the potential coexistence of ferroelectricity and magnetism. The ferroelectric transition temperature, ($T_C \sim 473$ K), of $YCrO_3$ compound is much higher than that of the antiferromagnetic (AFM) phase transition of Cr^{3+} ions ($T_N^{Cr} \sim 141.5K$) (Serrao et al., 2005; Zhu et al., 2020a). An isosymmetric structural phase transition was observed at ~ 900 K in a neutron powder diffraction study on the pulverized $YCrO_3$ single crystal, where

[1]Joint Key Laboratory of the Ministry of Education, Institute of Applied Physics and Materials Engineering, University of Macau, Avenida da Universidade, Taipa, Macao SAR 999078, China

[2]Department of Physics, City University of Hong Kong, Kowloon, Hong Kong SAR 999077, China

[3]State Key Laboratory of High Performance Ceramics and Superfine Microstructure, Shanghai Institute of Ceramics, Chinese Academy of Sciences, Shanghai 200050, China

[4]Guangdong–Hong Kong–Macao Joint Laboratory for Neutron Scattering Science and Technology, No. 1. Zhongziyuan Road, Dalang, DongGuan 523803, China

[5]These authors contributed equally

[6]Lead contact

*Correspondence:
yujianding@mail.sic.ac.cn (J.Y.),
aprqz@cityu.edu.hk (R.Z.),
haifengli@um.edu.mo (H.-F.L.)
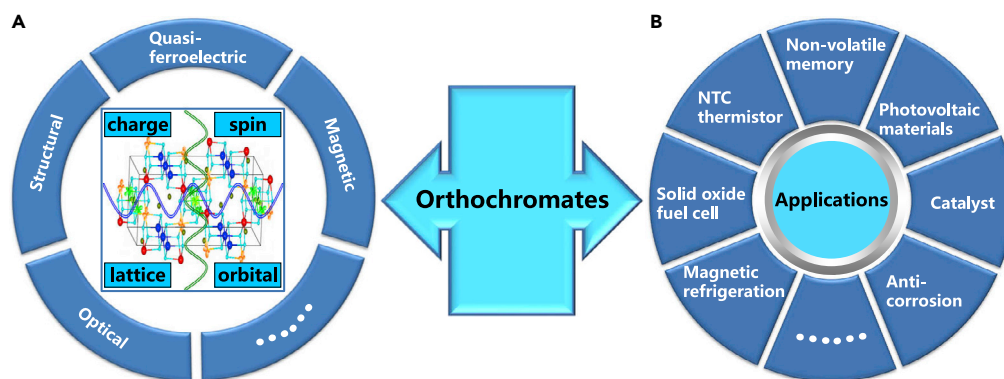
https://doi.org/10.1016/j.isci.2022.104111

Figure 1. Properties and applications of orthochromates

(A) Orthochromates display some interesting properties such as quasiferroelectric, structural, magnetic, and optical, resulting from couplings between charge, spin, orbital, and lattice degrees of freedom.

(B) These make orthochromates potential as magnetic refrigeration, solid oxide fuel cell, negative-temperature-coefficient (NTC) thermistor, nonvolatile memory application, photovoltaic materials, catalyst, and anticorrosion field.

the incompressibility of lattice constants a, b, and c is anisotropic, and there exist obvious atomic displacement and charge subduction on the Y and O2 sites (Zhu et al., 2020b). Net electric polarization was observed for polycrystalline $LuCrO_3$ and $ErCrO_3$ samples below T_N^{Cr}, indicating the presence of a possible ferroelectric state, whereas this is clearly absent above T_N^{Cr}. Most importantly, the study demonstrates that the paramagnetic (PM) nature of RE sites is not necessary to accommodate the ferroelectricity in orthochromates (Preethi Meher et al., 2014). In addition, the polarizations attain maximum values of $\sim 90 \ \mu C/m^2$ (at $E = 165$ kV/cm for $LuCrO_3$ compound) and $\sim 70 \ \mu C/m^2$ (at $E = 174$ kV/cm for $ErCrO_3$ compound). Both polarizations are reversal and can be explained by either the Cr^{3+} off-centering or the ferroelasticity or their couplings and even by Cr^{3+} vacancies (Preethi Meher et al., 2014). The $SmCrO_3$ compound demonstrates an electric polarization with the maximum value of $\sim 8 \ \mu C/m^2$ at $E = 1.43$ kV/cm and ~ 15 K (El Amrani et al., 2014), which was ascribed to a breaking of the local symmetry via Cr^{3+} off-centering (El Amrani et al., 2014). It was observed that electric dipoles exist in the $DyCrO_3$ compound, which was attributed to the displacement of Cr^{3+} cations (Yin et al., 2018). Electric polarizations were observed in $TbCrO_3$ and $TmCrO_3$ compounds at $E = 1.43$ kV/cm below T_N^{Cr} (Rajeswaran et al., 2012), whereas the existence of electric dipoles in the $TmCrO_3$ compound remains a debate (Yoshii and Ikeda, 2019).

Most previous studies focused on polycrystals, nanocrystals, and thin films. Single crystal growths of rare-earth orthochromates utilize mainly two methods: (i) one is the flux method (Yin et al., 2015). Unfortunately, impurities from the flux exist in the grown single crystals and have strong effects on macroscopic properties of the host (Cooke et al., 1974; Li et al., 2021; Looby and Katz, 1954; Zhu et al., 2020c). In addition, single crystals grown by the flux method are small, normally millimeter in size, and not suitable for some studies that make excessive demands in sample's quality and mass. (ii) The other is the floating-zone (FZ) method with a mirror furnace. Unfortunately, the intense volatility of Cr element because of its high vapor pressure at melting points of orthochromates (Philipp et al., 2003) can practically reduce the heating power of the mirror furnace (Li, 2008). This makes it not so easy to stably grow the single crystals of orthochromates. As a consequence, the lack of large single crystals has been a long-standing obstacle for studying their intrinsic properties and realizing some potential applications of orthochromates.

One of the long-standing unsolved issues existing in the family of $RECrO_3$ orthochromates is the microscopic origin of the weak ferromagnetism. This is introduced by the canted AFM structure. The Cr^{3+} state ($t_{2g}^3 e_g^0$) in orthochromates enables a virtual charge transfer (VCT) of $Cr^{3+} (t_{2g\uparrow}^3) - O^{2-} - Cr^{3+} (e_g^0)$ and a possible ferromagnetic (FM) competition with superexchange interactions $J \sim b^2/U$ (Landron and Lepetit, 2008), where b is the overlapping integral, and U denotes the on-site Coulomb interactions (Slater and Koster, 1954; Zhou et al., 2010). The overall Cr-O-Cr superexchange comprises two major contributions: One is from the $t_{2g} - t_{2g}$ hopping, producing an AFM component; the other is from the $t_{2g} - e_g$ orbital hybridization, generating FM couplings. The hybridization strength depends on the lattice distortion (Siddique et al., 2021), on-site Coulomb interaction (Besbes et al., 2019; Yekta et al., 2021), and $t_{2g} - e_g$ crystal field

splitting (Ko et al., 2007). The spin-orbit coupling induced Dzyaloshinskii-Moriya (DM) exchange would favor a magnetic structure with spins perpendicular to each other to minimize the total energy of the system (Coffey et al., 1991; Dmitrienko et al., 2014). To describe the effect of RE sites on the Cr^{3+}-O^{2-}-Cr^{3+} superexchange interactions, one can utilize density functional theory (DFT) based first-principles calculations to optimize the atomic information and correlate it with the superexchange interactions in $RECrO_3$ compounds. This provides a quantitative description of the t-e hybridization process. In addition, the AFM transition temperatures can be further calculated for a qualitative comparison to those measured from the grown single crystals.

In this paper, we report on a successful single crystal growth of the family of $RECrO_3$ compounds by a laser-diode FZ technique. Large single crystals measuring centimeters in size were obtained with the largest mass >10 g. The results from in-house characterizations on grown single crystals are in agreement with those from our first-principles calculations. Our research reveals that the t-e hybridization process can be tuned by RE-ions and induce FM interactions in the main AFM matrix and sheds light on the coexistence of weak ferromagnetism with antiferromagnetism and ferroelectricity in orthochromates.

RESULTS

Grown single crystals

Single-crystal materials hold translational symmetry of long-range building blocks; therefore, they provide reliable information of structures and properties of matters (Cheng, 2017; Li et al., 2018; Sun et al., 2019; Xiong et al., 2021; Zhang, 2020). Exploring and optimizing the single crystal growth parameters are time-consuming and labor-intensive processes (Li, 2008). For the first time, we have grown large single crystals of the family of $RECrO_3$ (RE = Y, Eu, Gd, Tb, Dy, Ho, Er, Tm, Yb, and Lu) compounds. Photos of some representative single crystals as-grown are exhibited in Figures 2A and 2B, where the $YbCrO_3$ (Figure 2A, ~ 7 cm in length) and $LuCrO_3$ (Figure 2B, ~ 10 cm) crystals have a diameter of $\varphi = 6 - 8$ mm and very shining surfaces. So far, the largest single crystal of orthochromates we have grown is >10 g for the $EuCrO_3$ compound. Our crystal growth engineering of $RECrO_3$ compounds produced a China invention patent (Li et al., 2021).

Neutron Laue diffraction patterns

We investigated the grown single crystals with a neutron Laue diffraction study. The top panels of Figures 2C–2E show the monitored neutron Laue patterns of a $YCrO_3$ single crystal with the three axes perpendicular to the paper: a axis (Figure 2C), b axis (Figure 2D), and c axis (Figure 2E). All patterns display symmetric and very strong diffraction spots, indicating a good quality of the grown single crystal. As shown in the bottom panels of Figures 2C–2E, we theoretically simulated the three patterns by using the OrientExpress software (Ouladdiaf et al., 2006), which further confirmed the good quality of our single crystals.

Magnetic properties

To clearly show features of dc magnetization in the vicinity of magnetic phase transitions, we present temperature-dependent data in the temperature range of 1.8–200 K. For the whole-temperature data (1.8–400 K), please refer to Figure S1. We measured the zero-field cooling (ZFC) magnetization at zero applied magnetic field, trying to explore the negative magnetization behavior and address whether the observed weak ferromagnetism is spontaneous.

We measured the ZFC magnetization data at 1000 Oe in the temperature range of 250–350 K and calculated the inverse magnetic susceptibility $\chi^{-1} = B/M$, which can well fit with the Curie-Weiss (CW) law for a pure paramagnetic (PM) state (Li et al., 2006, 2007, 2009; Zhu et al., 2020b),

$$\chi^{-1}(T) = \frac{3k_B(T - \Theta_{CW})}{N_A\mu_{eff}^2},$$

(Equation 1)

where k_B= 1.38062 × 10^{-23} J/K is the Boltzmann constant, Θ_{CW} is the PM CW temperature, N_A = 6.022 × 10^{23} mol^{-1} is Avogadro's constant, and μ_{eff} is the effective PM moment. We fit the data to Equation (1), extracting experimental values of the AFM transition temperature T_N^{Cr}, Θ_{CW}, and $\mu_{eff-meas}$ of $RECrO_3$ single crystals. These measured values were listed in Table 1. For the $RECrO_3$ compounds, it is pointed out that both RE^{3+} and Cr^{3+} ions contribute to the effective PM moment; therefore, the theoretical total
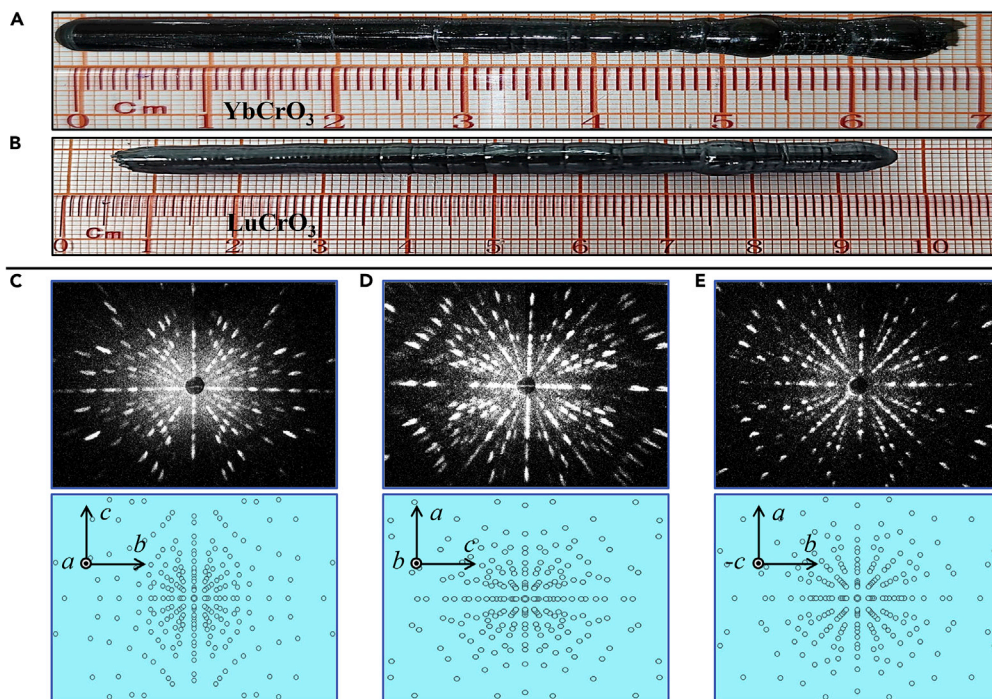
Figure 2. As-grown single crystals and neutron Laue diffraction patterns
(A) Photograph of a YbCrO$_3$ single crystal.
(B) Photograph of a LuCrO$_3$ single crystal as grown by a laser-diode FZ furnace.
(C–E) Neutron Laue patterns of single-crystal YCrO$_3$ (top panels) and the corresponding theoretical simulations (bottom panels). The real-space lattice vectors are marked in the bottom panels, and the crystallographic a axis (C), b axis (D), and c axis (E) are perpendicular to the paper.

effective PM moment $\mu_{eff-theo}^{total} = \sqrt{\left(\mu_{eff-theo}^{RE}\right)^2 + \left(\mu_{eff-theo}^{Cr}\right)^2}$, where $\mu_{eff-theo}^{RE} = g\mu_B\sqrt{J(J+1)}$, and $\mu_{eff-theo}^{Cr} = g\,\mu_B\sqrt{S(S+1)} = 3.873\,\mu_B$ (where $S = 3/2$). The quantum numbers of RE^{3+} and Cr^{3+} ions and the calculated values of $\mu_{eff-theo}^{RE}$ and $\mu_{eff-theo}^{total}$ were listed in Table 1 for a comparison to the corresponding experimental values. Within 250–350 K, the fits coincide well with the measured magnetization of RECrO$_3$ (RE = Eu, Tb, Dy, Ho, Er, Tm, Yb, and Lu) single crystals. As temperature decreases from 250 to 220 K, the measured data did not show obvious deviation from the Curie-Weiss law fitting (short-dashed line), which confirms the validity of our theoretical fits and that the RECrO$_3$ (RE = Eu, Tb, Dy, Ho, Er, Tm, Yb, and Lu) single crystals remain a pure PM state in the temperature range of 220–350 K.

Magnetic hysteresis loops at the low-field regimes were measured. The isothermal field dependence of magnetization with applied magnetic field from –14 to 14 T was supplemented in Figure S2.

In the following, we present analyses of the magnetic properties of RECrO$_3$ (RE = Eu, Tb, Dy, Ho, Er, Tm, Yb, and Lu) single crystals one by one.

EuCrO$_3$

EuCrO$_3$ demonstrates negative magnetization behavior at zero magnetic field below T_N^{Cr} (Figure 3A), whereas the ZFC magnetization at B = 50 Oe increases sharply below T_N^{Cr} within a thermal regime of $\sim$ 1.2 K and then flattens to 1.8 K upon cooling. The field-cooling (FC) magnetization at 100 Oe increases by $\sim$ 18% at 1.8 K. The magnetization measured at 50 and 100 Oe resembles the features of a weak FM state. We determined that $T_N^{Cr} = 181.6(1)$ K for a EuCrO$_3$ single crystal. Below T_N^{Cr} EuCrO$_3$ enters a canted AFM state, probably because of the Dzyaloshinskii-Moriya interactions of Cr^{3+} ions.

To avoid the effect of non-intrinsic magnetic contributions at low applied magnetic fields, we used the ZFC magnetization measured from 250 to 350 K at 1000 Oe for CW fitting (Figure 3B). This produces an effective

Table 1. Calculated theoretical quantum numbers of RE^{3+} ions in $RECrO_3$ single crystals based on the Hund's rule: number of $4f$ ($4d$ for Y^{3+} ion) electrons, spin S, orbital L, total angular momentum J, Landé factors g_J, and the ground-state term $^{2S+1}L_J$

		$RECrO_3$ single crystals grown by the FZ method			
RE^{3+} =	Y^{3+}	Eu^{3+}	Gd^{3+}	Tb^{3+}	Dy^{3+}
$4d^n$ ion	0				
$4f^n$ ions		6	7	8	9
S	0	3	7/2	3	5/2
L	0	3	0	3	5
J	0	0	7/2	6	15/2
g_J	–	–	2	1.5	1.33
$^{2S+1}L_J$	$^1S_0$	$^7F_0$	$^8S_{7/2}$	$^7F_6$	$^6H_{15/2}$
$\mu_{eff-meas}(\mu_B)$	3.95	6.44	8.40	10.51	11.35
$\mu_{eff-theo}^{RE}(\mu_B)$	0	0	7.937	9.721	10.646
$\mu_{eff-theo}^{total}(\mu_B)$	3.873	3.873	8.832	10.464	11.328
$M_{meas}(\mu_B)$	~0.147	0.245 (1)	6.43	6.248 (1)	4.834 (1)
$M_{sat-theo}^{RE}(\mu_B)$	0	0	7	9	10
$M_{sat-theo}^{total}(\mu_B)$	3	3	7.616	9.487	10.440
T_N (K)	141.5 (1)	181.6 (1)	169.3 (1)	157.9 (1)	148.5 (1)
θ_{CW} (K)	−433.2 (6)	−450.4 (15)	−20.33 (4)	−53.3 (1)	−56.5 (1)
RE^{3+} =	Ho^{3+}	Er^{3+}	Tm^{3+}	Yb^{3+}	Lu^{3+}
$4f^n$ ion	10	11	12	13	14
S	2	3/2	1	1/2	0
L	6	6	5	3	0
J	8	15/2	6	7/2	0
g_J	1.25	1.2	1.167	1.143	–
$^{2S+1}L_J$	$^5I_8$	$^4I_{15/2}$	$^3H_6$	$^2F_{7/2}$	$^1S_0$
$\mu_{eff-meas}(\mu_B)$	11.03	10.20	8.35	5.63	4.98
$\mu_{eff-theo}^{RE}(\mu_B)$	10.607	9.581	7.561	4.536	0
$\mu_{eff-theo}^{total}(\mu_B)$	11.292	10.334	8.495	5.964	3.873
$M_{meas}(\mu_B)$	3.999 (1)	6.385 (1)	2.868 (1)	0.883 (1)	1.197 (1)
$M_{sat-theo}^{RE}(\mu_B)$	10	9	7	4	0
$M_{sat-theo}^{total}(\mu_B)$	10.440	9.487	7.616	5	3
T_N (K)	143.2 (1)	135.4 (1)	125.9 (1)	117.9 (1)	122.3 (1)
θ_{CW} (K)	19.6 (1)	−30.0 (1)	−90.6 (4)	−17.4 (1)	−110.4 (2)

We listed values of the measured (meas) ($\mu_{eff-meas}$) and theoretical (theo) effective PM moments $\left(\mu_{eff-theo}^{Cr} = g_J\mu_B\sqrt{S(S+1)} = 3.873 \ \mu_B\left(Cr^{3+}: 3d^3, J = S = \frac{3}{2};\right.\right.$ $\left.g_J = 2\right), \mu_{eff-theo}^{RE} = g_J\mu_B\sqrt{J(J+1)}$, and $\mu_{eff-theo}^{total} = \sqrt{\left(\mu_{eff-theo}^{RE}\right)^2 + \left(\mu_{eff-theo}^{Cr}\right)^2}$, the measured moment ($M_{meas}$ per formula at 1.8 K and 14 T), and the theoretical saturation moments ($M_{sat-theo}^{Cr} = g_J\mu_B S = 3\mu_B, M_{sat-theo}^{RE} = g_J\mu_B J$, and $M_{sat-theo}^{total} = \sqrt{\left(M_{sat-theo}^{RE}\right)^2 + \left(M_{sat-theo}^{Cr}\right)^2}$. The values of $T_N, \mu_{eff-meas}$, and CW temperature (θ_{CW}) were extracted from the $M-T$ measurements by the CW-law fitting. The values of M_{meas} were extracted from the $M-B$ data. The numbers in parenthesis are the estimated standard deviations of the (next) last significant digit. Some parameters of $YCrO_3$ (Zhu et al., 2020a) and $GdCrO_3$ (Zhu et al., 2020c) were referred to in our previous studies.

PM moment $\mu_{eff-meas} = 6.44 \ \mu_B$, which is considerably larger than the theoretical value $\mu_{eff-theo}^{total} = 3.873 \ \mu_B$ (Table 1) and a CW temperature $\Theta_{CW} = -450.4(15)$ K.

The field dependence of magnetization measured at 1.8 K is displayed in Figure 3C, where clear magnetic hysteresis loops are observed at 1.8 and 20 K, and there is nearly no difference between them. Remanent magnetization $M_r \sim 0.91$ emu g^{-1} and coercive field $B_c \sim 95$ Oe were determined. The magnetic hysteresis loop closes at ~ 867 Oe, after which the ZFC magnetization increases linearly as a function of the magnetic field, with a slope of dM/dB= 0.322(1) emu g^{-1} T^{-1} (Figure S2A). Given that the theoretical saturation
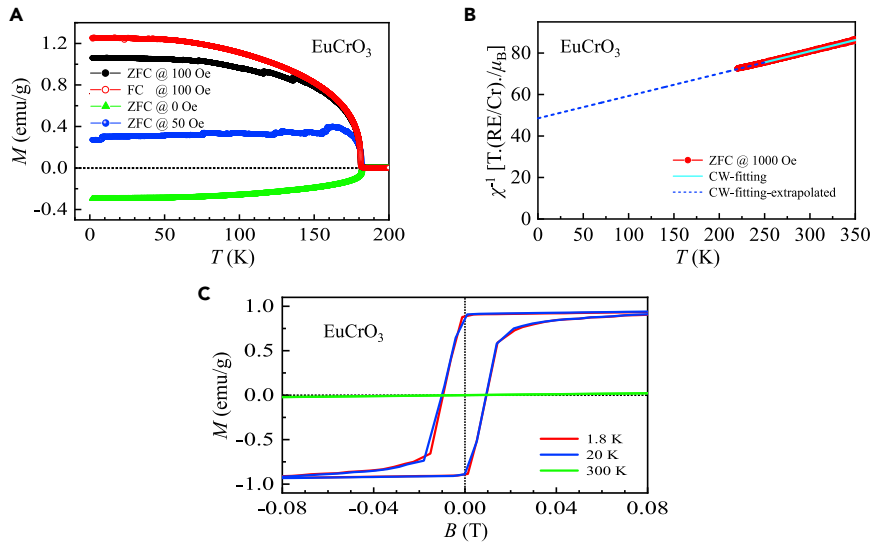
Figure 3. Magnetic property of EuCrO₃

(A) Magnetization as a function of temperature from 1.8–200 K measured at 0, 50, and 100 Oe. We performed both zero-field and field-cooling measurements at 100 Oe.

(B) Zero-field cooling inverse magnetic susceptibility χ^{-1} (solid circles) at an applied magnetic field of 1000 Oe as a function of temperature in the range of 220–350 K. The solid lines represent the fits with a Curie-Weiss law from 250–350 K. The Curie-Weiss law fits were extrapolated to low temperatures shown as short-dashed lines.

(C) Magnetic hysteresis loops measured at low applied magnetic fields with selected temperatures.

magnetic moment of Cr^{3+} ions is $M_{sat-theo}^{Cr} = g_J \mu_B S = 3 \mu_B$, where $g_J = 2$ and $S = \frac{3}{2}$ for pure ionic Cr^{3+} ions (Table 1), it is inferred that attaining a full magnetic saturation state requires $B \approx 203$ T. At 1.8 K and 14 T, a magnetization of $M_{meas} = 0.245$ (1) μ_B/Cr was reached (Figure S2A), which is equal to $\sim 8.2\%$ of the theoretical value $M_{sat-theo}^{total} = 3\mu_B$/Cr.

Our study indicates a possible existence of competition between FM and AFM exchange interactions. We did not observe the magnetic ordering of Eu^{3+} ions, which is consistent with a previous study on polycrystalline EuCrO₃ samples (Taheri et al., 2016).

TbCrO₃

We determined that $T_N^{Cr} = 157.9(1)$ K for a TbCrO₃ single crystal (Figure 4A). Below T_N^{Cr}, the ZFC magnetization at 0 Oe was negative, whereas the magnetization curves at 50 and 100 Oe increased gradually after a sharp enhancement around T_N^{Cr} within ~ 0.56 K. Below ~ 70 K, the ZFC magnetization at 100 Oe evidently exceeded that measured at 50 Oe. At ~ 7.7 K, a kink appeared in the magnetization at 50 and 100 Oe (ZFC at 50 and 100 Oe: downturn; FC at 100 Oe: uturn), indicating the formation of Tb^{3+} spin ordering. Below ~ 4.5 K, a sharp decrease in the magnetization at 50 and 100 Oe and a sharp increase in that at 0 Oe were observed. Below ~ 3 K, the ZFC magnetization at 0, 50, and 100 Oe approached zero. Therefore, we observe elaborate magnetic phase transitions with temperature in the TbCrO₃ single crystal.

The CW fitting result of $\mu_{eff-meas} = 10.51$ μ_B (Figure 4B) is nearly equal to the theoretical value $\mu_{eff-theo}^{total} = 10.464$ μ_B. The CW temperature $\Theta_{CW} = -53.3(1)$ K indicates a weak competition between the FM and AFM interactions in our TbCrO₃ single crystal.

A clear magnetic hysteresis loop was observed with $M_r \sim 2.75$ emu g⁻¹ and $B_c \sim 48$ Oe at 15 K (Figure 4C), indicating a weak FM state of the Cr^{3+} ions. When $T = 1.8$ K, both Tb^{3+} and Cr^{3+} spins order, and the observed magnetization loop was stretched along the B axis and squeezed along the magnetization axis, leading to a parallelogram-shaped hysteresis loop with $M_r \sim 1.82$ emu g⁻¹ and $B_c \sim 2500$ Oe (Figure 4C). Such a twisted loop has not been previously observed in either polycrystalline or single-crystalline (grown by the flux method) samples (Vagadia et al., 2018; Yin et al., 2016). This indicates a stronger coupling between the Cr^{3+} and Tb^{3+} spins in our TbCrO₃ single crystal. As B increased, the loop at 1.8 K gets a quick saturation at $B_s \sim 1.67$ T, whereas that at 15 K increased
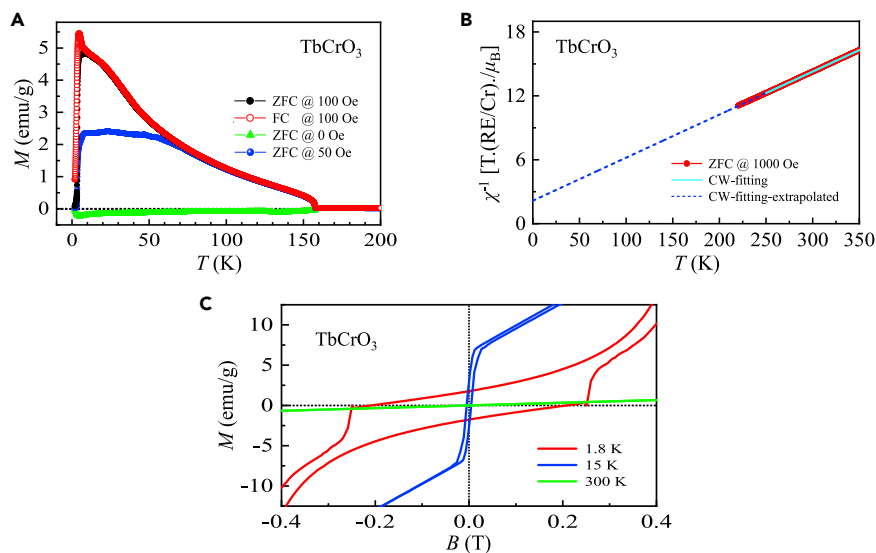
Figure 4. Magnetic property of TbCrO$_3$

(A) Magnetization as a function of temperature from 1.8–200 K measured at 0, 50, and 100 Oe. We performed both zero-field and field-cooling measurements at 100 Oe.

(B) Zero-field cooling inverse magnetic susceptibility χ^{-1} (solid circles) at an applied magnetic field of 1000 Oe as a function of temperature in the range of 220–350 K. The solid lines represent the fits with a Curie-Weiss law from 250–350 K. The Curie-Weiss law fits were extrapolated to low temperatures shown as short-dashed lines.

(C) Magnetic hysteresis loops measured at low applied magnetic fields with selected temperatures.

smoothly and attained a plateau at ~ 6.8 T. At 1.8 K and 14 T, the magnetization reached $M_{meas} = 6.248(1)$ μ_B, which is $\sim 34\%$ smaller than the theoretical value $M_{sat-theo}^{total} = 9.487$ μ_B (Table 1).

TbCrO$_3$ entered a long-range canted AFM state of Cr^{3+} ions below $T_N^{Cr} = 157.9(1)$. The possible long-range AFM order of Tb^{3+} ions was formed below $T_N^{Tb} \sim 7.7$ K. Strong coupling was observed between the spin orders of the Cr^{3+} and Tb^{3+} ions. In addition, a weak competition between the FM and AFM interactions of the Cr^{3+} ions was observed.

DyCrO$_3$

The DyCrO$_3$ single crystal underwent a magnetic phase transition from the PM state to a canted AFM phase at $T_N^{Cr} = 148.5(1)$ K. (Figure 5A), corresponding to the formation of Cr^{3+} spin ordering. A kink appeared at $T_{SR}^{Cr} \sim 38$ K in the magnetization at 0, 50, and 100 Oe (Figure 5B), which is attributed to the spin reorientation of the Cr ions. A similar observation was previously reported for DyCrO$_3$ single crystals grown by the flux method, where the appearance of the kink was believed to be caused by the spin reorientation of Dy^{3+} ions (Yin et al., 2016). Below T_N^{Cr}, the magnetization increased smoothly until the onset of a sharp enhancement at ~ 17 K, reaching a maximum at ~ 2.54 K and then followed by a quick reduction. Therefore, we observed an AFM phase transition of the Dy^{3+} ions at $T_N^{Dy} \sim 2.8$ K.

The CW fitting produces $\mu_{eff-meas} = 11.35$ μ_B (Figure 5C), which is nearly equal to the theoretical value $\mu_{eff-theo}^{total} = 11.328\mu_B$. CW temperature, $\Theta_{CW} = -56.5(1)$ K (Table 1).

Isothermal magnetic hysteresis loops were observed at 1.8 ($M_r \sim 4.7$ emu g^{-1}; $B_c \sim 639$ Oe) and 10 K ($M_r \sim 1.1$ emu g^{-1}; $B_c \sim 41$ Oe) (Figure 5D), confirming that Cr^{3+} spins hold a canted AFM state. For the Dy^{3+} sub-lattices, we could only conclude that the spins form an AFM state. At both 1.8 and 10 K, the magnetization curves finally flattened with $M_{meas} = 4.834$ (1) μ_B at 14 T (Figure S2C). This value was $\sim 53.7\%$ less than the theoretical value of $M_{sat-theo}^{total} = 10.440$ μ_B (Table 1).

HoCrO$_3$

We determined that $T_N^{Cr} = 143.2(1)$ K for a HoCrO$_3$ single crystal (Figure 6A). Below T_N^{Cr}, the ZFC magnetization at 0 Oe was negative, whereas those at 50 and 100 Oe were positive and increased smoothly in the
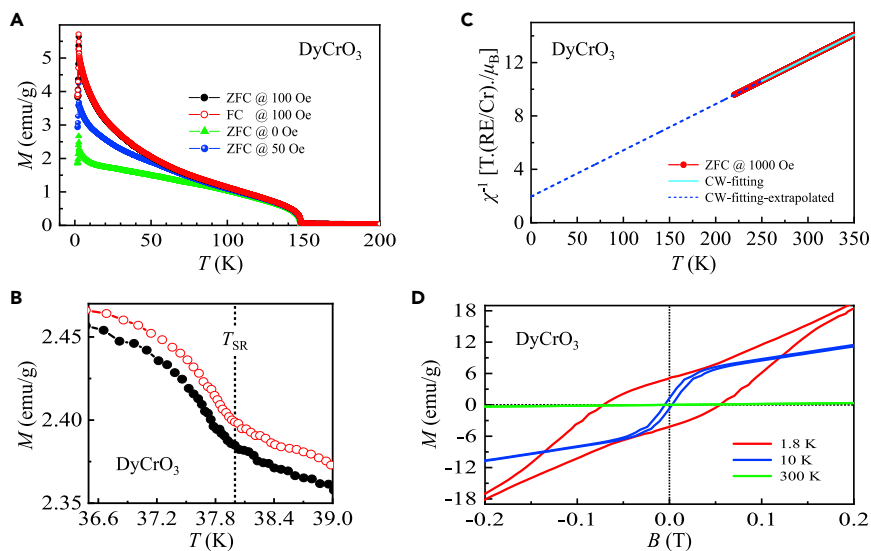
Figure 5. Magnetic property of DyCrO₃

(A) Magnetization as a function of temperature from 1.8–200 K measured at 0, 50, and 100 Oe. We performed both zero-field and field-cooling measurements at 100 Oe.

(B) Schematically showing the determination of the spin-reorientation temperature T_{SR}.

(C) Zero-field cooling inverse magnetic susceptibility χ^{-1} (solid circles) at an applied magnetic field of 1000 Oe as a function of temperature in the range of 220–350 K. The solid lines represent the fits with a Curie-Weiss law from 250–350 K. The Curie-Weiss law fits were extrapolated to low temperatures shown as short-dashed lines.

(D) Magnetic hysteresis loops measured at low applied magnetic fields with selected temperatures.

temperature regimes of $\sim$ 19 K (at 50 Oe) and $\sim$ 47 K (at 100 Oe) and then flatten until $T_N^{Ho} \sim 7.82$ K, at which Ho³⁺ ions order antiferromagnetically. Below $\sim$ 2.4 K, all curves were flattened. When 2.4 K$<T<T_N^{Ho}$, the magnetization curves at ZFC (down turn) and FC (up turn) 100 Oe demonstrated an inverse trend; above T_N^{Ho}, they coincided. The degree of canting of the Cr³⁺ AFM structure determines the strength of the resulting ferromagnetism along the c axis. This prevents the formation of an AFM structure of the Ho³⁺ ions. The difference between the ZFC and FC magnetization at 100 Oe is controlled by the competition between the Zeeman energy generated by the applied magnetic field, crystal field, AFM interaction strength of Ho³⁺ ions, and magnetic anisotropy (Li, 2016).

We obtained $\mu_{eff-meas}$ = 11.03 μ_B, which is comparable to $\mu_{eff-theo}^{total}$ = 11.292 μ_B, and Θ_{CW} = 19.6(1) K (Figure 6B and Table 1). The previous study on polycrystalline HoCrO₃ sample shows $\mu_{eff-meas}$ = 11.55 μ_B and Θ_{CW} = $-$ 24.0 K (Su et al., 2011). Obtaining evidence of short-range exchange interactions and magnetic fluctuations of Ho³⁺ spins reported previously by quasielastic and inelastic neutron scattering studies on HoCrO₃ powder samples (Chatterji et al., 2017; Kumar et al., 2016) necessitates more in-house characterizations with the HoCrO₃ single crystal.

At 1.8 and 15 K, we observed magnetic hysteresis loops in step-increasing mode (Figure 6C). We extracted $M_r \sim 3.5$ (1.8 K) and 1.9 (15 K) emu g⁻¹ and the corresponding $B_c \sim 140$ and 72 Oe, respectively. At 15 K, the magnetization increased linearly at B $\leq$ 618 Oe and then proceeded smoothly into a plateau at $\sim$ 3.2 T; in contrast, at 1.8 K and B $\leq$ 1092 Oe, the magnetization almost increased linearly with increasing magnetic field and then attained M_{meas} = 3.999(1) μ_B at 14 T (Figure S2D). This value was only $\sim$ 38.3% of the theoretical value $M_{sat-theo}^{total}$ = 10.440μ_B (Table 1).

ErCrO₃

Below T_N^{Cr} = 135.4(1) K (Eibschütz et al., 1970), there was a small sharp enhancement in the magnetization within $\sim$ 0.72 K, which then increased smoothly until an onset of a sudden decrease at $T_{SR}^{Cr} \sim 9.7$ K (Figure 7A). The decrease in magnetization is attributed to the spin reorientation of Cr³⁺ ions from $\Gamma_4(G_x, A_y, F_z; F_z^R)$ to $\Gamma_1(A_x, G_y, C_z; C_z^R)$ or the $\Gamma_1(0)$ spin configuration (Su et al., 2010b, 2012). Below
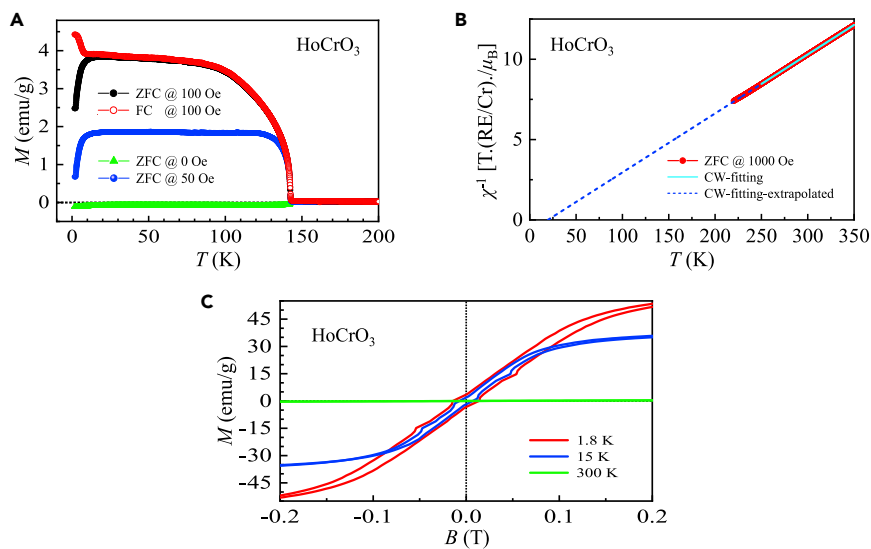
Figure 6. Magnetic property of HoCrO₃

(A) Magnetization as a function of temperature from 1.8–200 K measured at 0, 50, and 100 Oe. We performed both zero-field and field-cooling measurements at 100 Oe.

(B) Zero-field cooling inverse magnetic susceptibility χ^{-1} (solid circles) at an applied magnetic field of 1000 Oe as a function of temperature in the range of 220–350 K. The solid lines represent the fits with a Curie-Weiss law from 250–350 K. The Curie-Weiss law fits were extrapolated to low temperatures shown as short-dashed lines.

(C) Magnetic hysteresis loops measured at low applied magnetic fields with selected temperatures.

$T_N^{Er} \sim 8$ K, the magnetization at 0, 50, and 100 Oe decreased linearly. No difference was found in the ZFC and FC magnetization at 100 Oe.

The CW fitting resulted in an effective PM magnetic moment of 10.20 μ_B, in agreement with the theoretical value of 10.334 μ_B, and a CW temperature of $-30.0(1)$ K (Figure 7B and Table 1).

No magnetic hysteresis loop appeared in the M-B measurements (Figure 7C). In contrast, clear hysteresis loops were observed previously for polycrystalline ErCrO₃ samples (Shi et al., 2018). For the magnetization curve at 1.8 K, a gate magnetic field of ~ 650 Oe existed. When $0 \leq B \leq B_{gate} = 650$ Oe, the magnetization increased linearly from 0 to ~ 0.45 emu g^{-1}. Then, it quickly flattened when $B \sim 0.617$ T and attained $M_{meas} = 6.385(1)$ μ_B at 14 T (Figure S2E).

TmCrO₃

We determined that $T_N^{Cr} = 125.9(1)$ K for the TmCrO₃ single crystal (Figure 8A), which is consistent with a previous study of polycrystalline TmCrO₃ (Wang et al., 2016a; Yoshii, 2012). Below T_N^{Cr}, the ZFC magnetization at 0 Oe was negative. The magnetization at 50 and 100 Oe was positive and increased sharply within ~ 1 K. This is because Cr^{3+} spins order into a canted AFM state of the Γ_2 configuration ($F_x C_y G_z$) (Tamaki et al., 1977; Yoshii, 2012). Upon further cooling, the magnetization increased smoothly until it reached a maximum at $T_{max}^{Cr} \sim 74$ K. After that, the magnetization reduced smoothly and attained negative values suddenly at $T_{SR} \sim 37.2$ K (for ZFC at 50 and 100 Oe) and ~ 40.1 K (for FC at 100 Oe), followed by a sharp increase with positive values appearing again at a compensation temperature $T_{comp} \sim 28.72$ K. The sharp drop observed at ~ 40.1 K could be ascribed to the spin reorientation of Cr^{3+} ions accompanied by a 90° rotation of the spins, that is, from one crystallographic axis to another, probably because of the competition between anisotropic exchanges and single-ion anisotropy (Li, 2016). This feature became smooth in the polycrystalline samples (Wang et al., 2016a; Yoshii, 2012). Our study revealed a reversal of the magnetization behavior. The ZFC and FC magnetization at 100 Oe nearly coincided with each other. This is different from the observations with polycrystalline TmCrO₃ (Yoshii, 2012). We observed a magnetic phase transition at $T_N^{Tm} \sim 19.6$ K, which probably correlates with the AFM order of Tm^{3+} ions. This was not observed in polycrystalline TmCrO₃ samples (Wang et al., 2016a; Yoshii, 2012).
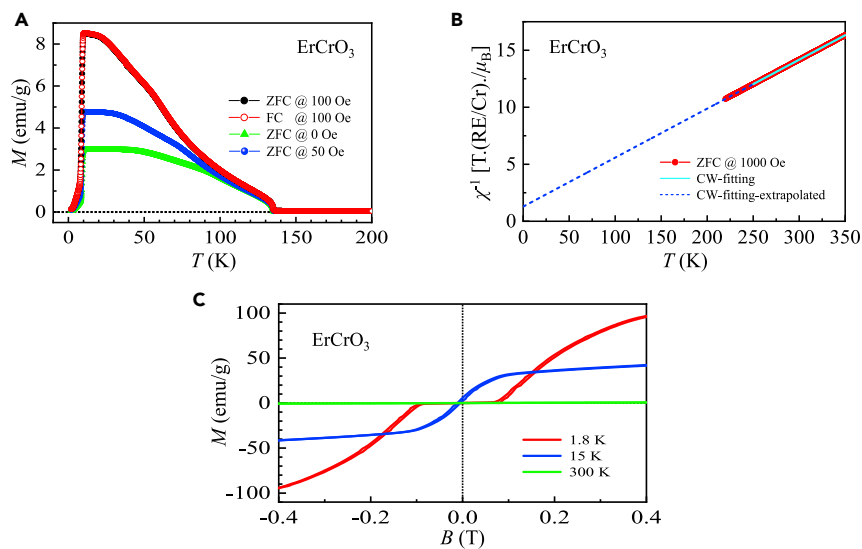
Figure 7. Magnetic property of ErCrO₃

(A) Magnetization as a function of temperature from 1.8–200 K measured at 0, 50, and 100 Oe. We performed both zero-field and field-cooling measurements at 100 Oe.

(B) Zero-field cooling inverse magnetic susceptibility χ^{-1} (solid circles) at an applied magnetic field of 1000 Oe as a function of temperature in the range of 220–350 K. The solid lines represent the fits with a Curie-Weiss law from 250–350 K. The Curie-Weiss law fits were extrapolated to low temperatures shown as short-dashed lines.

(C) Magnetic hysteresis loops measured at low applied magnetic fields with selected temperatures.

We obtained $\mu_{eff-meas}$ = 8.35 μ_B, which is almost identical to the theoretical value $\mu^{total}_{eff-theo}$ = 8.495 μ_B, and Θ_{CW} = − 90.6(4) K (Figure 8B and Table 1).

We observed different magnetic hysteresis loops (Figure 8C): (i) at 20 K, a parallelogram-shaped loop with $M_r \sim$ 1.4 emu g^{-1} and $B_c \sim$ 111 Oe. (ii) At 1.8 K, a twisted loop with $M_r \sim$ 0.75 emu g^{-1} and $B_c \sim$ 38.2 Oe. The magnetization reached M_{meas} = 2.868(1) μ_B at 14 T (Figure S2F and Table 1).

YbCrO₃

We determined that T^{Cr}_N = 117.9(1) K for the YbCrO₃ single crystal (Figure 9A), which is the lowest magnetic phase transition temperature of Cr^{3+} sublattices among all rare-earth orthochromates. Below T^{Cr}_N, the ZFC magnetization at 0 Oe reduced sharply to negative values, whereas the magnetization at 50 and 100 Oe increased sharply and attained the maximum values at $T^{Cr}_{max} \sim$ 99.3 K (for ZFC at 50 Oe), 86.3 K (for ZFC at 100 Oe), and 69.6 K (for FC at 100 Oe), followed by smooth decreases to negative values at compensation temperatures $T_{comp1} \sim$ 63.7 K (for ZFC at 50 Oe), 47.5 K (for ZFC at 100 Oe), and 15.5 K (for FC at 100 Oe). The positive values of magnetization at 0, 50, and 100 (ZFC) Oe reappeared at $T_{comp2} \sim$ 15.5 K (for ZFC at 0 Oe), 17.6 K (for ZFC at 50 Oe), and 19.5 K (for ZFC at 100 Oe), whereas the magnetization at FC 100 Oe still remained negative. Below $T^{Yb}_N \sim$ 7K, all the ZFC magnetization curves flattened (Su et al., 2010a). Notably, a large difference exists between the curves of the ZFC and FC magnetizations at 100 Oe. The FC magnetization at 100 Oe resembles that observed in the polycrystalline samples (Wang et al., 2016b).

The CW fitting resulted in $\mu_{eff-meas}$ = 5.63 μ_B, which was slightly lower than the theoretical value $\mu^{total}_{eff-theo}$ = 5.964 μ_B, and Θ_{CW} = − 17.4(4) K (Figure 9B and Table 1).

No magnetic hysteresis loop appeared in the ZFC *M-B* curves at 15 and 300 K, whereas we observed magnetic hysteresis loops with a similar shape at 1.8 K ($M_r \sim$ 0.24 emu g^{-1}; $B_c \sim$ 1200 Oe), 25 K ($M_r \sim$ 0.14 emu g^{-1}; $B_c \sim$ 1200 Oe), and 40 K ($M_r \sim$ 0.25 emu g^{-1}; $B_c \sim$ 1780 Oe) (Figure 9C). The measured magnetization M_{meas} = 0.883(1) μ_B at 1.8 K and 14 T, which is merely $\sim$ 17.7% of $M^{total}_{sat-theo}$ = 5μ_B (Figure S2G and Table 1).
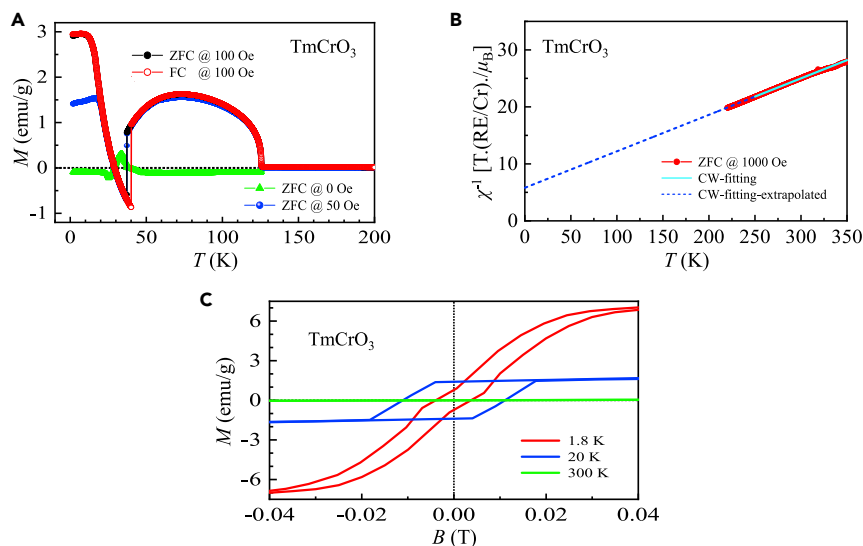
Figure 8. Magnetic property of TmCrO₃

(A) Magnetization as a function of temperature from 1.8–200 K measured at 0, 50, and 100 Oe. We performed both zero-field and field-cooling measurements at 100 Oe.

(B) Zero-field cooling inverse magnetic susceptibility χ^{-1} (solid circles) at an applied magnetic field of 1000 Oe as a function of temperature in the range of 220–350 K. The solid lines represent the fits with a Curie-Weiss law from 250–350 K. The Curie-Weiss law fits were extrapolated to low temperatures shown as short-dashed lines.

(C) Magnetic hysteresis loops measured at low applied magnetic fields with selected temperatures.

LuCrO₃

The LuCrO₃ single crystal exhibited magnetic behaviors similar to those observed in single-crystal TmCrO₃ (Figures 8A and 10A). We determined T_N^{Cr} = 122.3(1) K, $T_{max}^{Cr} \sim$ 79 K (for ZFC and FC at 100 Oe), $T_{SR} \sim$ 33 K (for ZFC at 50 Oe) and 31 K (for ZFC and FC at 100 Oe), $T_{comp2} \sim$ 28 K (for all data), and $T_N^{Lu} \sim$ 2.3 K for the
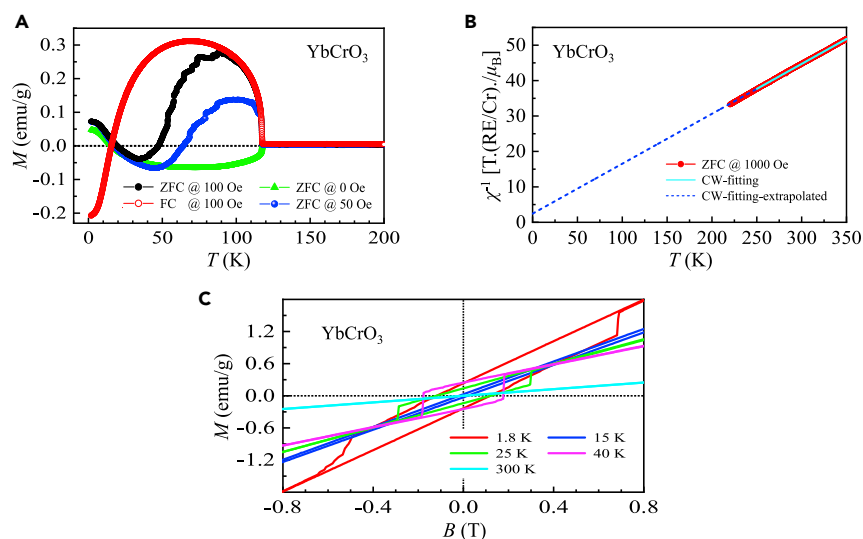

Figure 9. Magnetic property of YbCrO₃

(A) Magnetization as a function of temperature from 1.8–200 K measured at 0, 50, and 100 Oe. We performed both zero-field and field-coolings measurements at 100 Oe.

(B) Zero-field cooling inverse magnetic susceptibility χ^{-1} (solid circles) at an applied magnetic field of 1000 Oe as a function of temperature in the range of 220–350 K. The solid lines represent the fits with a Curie-Weiss law from 250–350 K. The Curie-Weiss law fits were extrapolated to low temperatures shown as short-dashed lines.

(C) Magnetic hysteresis loops measured at low applied magnetic fields with selected temperatures.

Figure 10. Magnetic property of LuCrO₃

(A) Magnetization as a function of temperature from 1.8–200 K measured at 0, 50, and 100 Oe. We performed both zero-field and field-cooling measurements at 100 Oe.

(B) Zero-field cooling inverse magnetic susceptibility χ^{-1} (solid circles) at an applied magnetic field of 1000 Oe as a function of temperature in the range of 220–350 K. The solid lines represent the fits with a Curie-Weiss law from 250–350 K. The Curie-Weiss law fits were extrapolated to low temperatures shown as short-dashed lines.

(C) Magnetic hysteresis loops measured at low applied magnetic fields with selected temperatures.
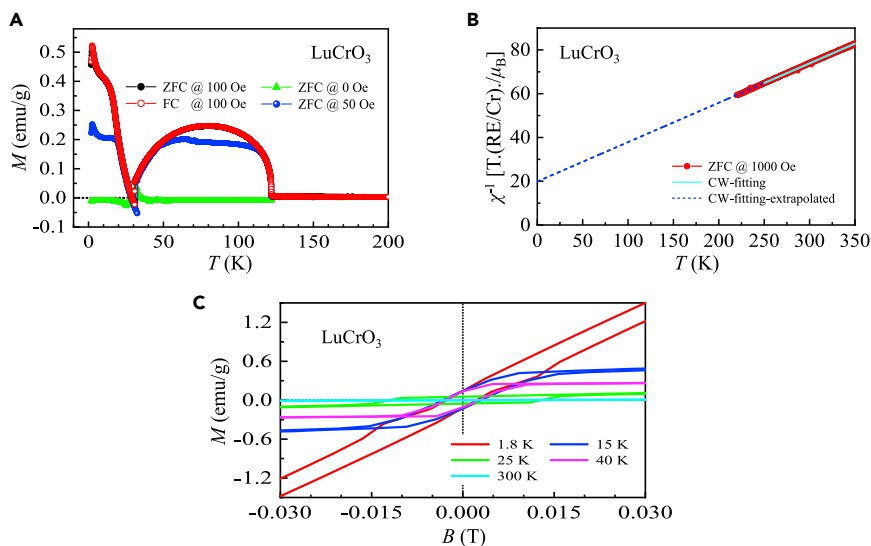
LuCrO₃ single crystal. No clear difference was observed in the ZFC and FC magnetization at 100 Oe. Our LuCrO₃ single crystal demonstrated magnetic behaviors different from those of previous polycrystalline samples (Durán et al., 2014).

The CW fitting results in $\mu_{eff-meas}$ = 4.98 μ_B, which is ∼ 28.1% higher than the theoretical value $\mu_{eff-theo}^{total}$ = 3.873μ_B, and Θ_{CW} = − 110.4(2)K (Figure 10B and Table 1).

We observed magnetic hysteresis loops at: 1.8 K (M_r ∼ 0.13 emu g^{-1}; B_c ∼ 25 Oe), 15 K (M_r ∼ 0.14 emu g^{-1}; B_c ∼ 32 Oe), 25 K (M_r ∼ 0.054 emu g^{-1}; B_c ∼ 125 Oe), and 40 K (M_r ∼ 0.12 emu g^{-1}; B_c ∼ 28 Oe) (Figure 10C). The measured magnetization, M_{meas} 1.197(1) μ_B, at 1.8 K and 14 T is merely ∼ 39.9% of $M_{sat-theo}^{total}$ = 3μ_B (Figure S2H and Table 1).

We summarize the magnetic behaviors of single-crystal RECrO₃ compounds as follows: (i) TbCrO₃, DyCrO₃, and ErCrO₃ displayed similar temperature dependencies as did TmCrO₃ and LuCrO₃ single crystals. (ii) DyCrO₃ and ErCrO₃ did not exhibit negative magnetization, whereas the others did. (iii) Reversal magnetic behaviors (positive → negative → positive) occurred for TmCrO₃, YbCrO₃, and LuCrO₃ single crystals. (iv) We did not observe any indication of Eu^{3+} magnetic ordering, which may require lower temperatures. (v) Obvious magnetic hysteresis loops were observed for RECrO₃, except for ErCrO₃. (vi) The measured magnetization at 1.8 K and high magnetic fields plateaued for RECrO₃ (RE = Tb, Dy, Ho, Er, and Lu) single crystals. (vii) The measured effective PM moments of EuCrO₃ and LuCrO₃ were not consistent with the theoretical values. (viii) The applied magnetic field of 14 T was far less to saturate RECrO₃ at 1.8 K. (ix) Only HoCrO₃ demonstrated a positive CW temperature. Finally, we observed the complex and coupled magnetic phase transitions of RE^{3+} (except for Eu^{3+}) and Cr^{3+} ions.

We also summarize the magnetic structures of RE^{3+} and Cr^{3+} ions in RECrO₃ (RE = Gd, Tb, Dy, Ho, Er, Tm, Yb, and Lu) compounds in the literature (Table 2). The magnetic SR transition of Cr^{3+} ions has been reported for GdCrO₃ (Cooke et al., 1974) and ErCrO₃ (Hornreich, 1978; Shamir et al., 1981) compounds. The detailed magnetic structures of Tm^{3+} and Yb^{3+} ions in TmCrO₃ (Shamir et al., 1981) and YbCrO₃ (Shamir et al., 1981) compounds remain controversial. A F_x magnetic component of Yb^{3+} ions had to be included for a satisfactory fit of the neutron powder diffraction data of YbCrO₃ in the temperature range

Table 2. Summary of the previously reported magnetic structures of RE^{3+} and Cr^{3+} ions in $RECrO_3$ (RE = Gd, Tb, Dy, Ho, Er, Tm, Yb, and Lu) compounds

$RECrO_3$	RE^{3+} ($T < T_N^{RE}$)	Cr^{3+} ($T < T_{SR}^{Cr}$)	SR (Cr^{3+})	Cr^{3+} ($T_{SR}^{Cr} < T < T_N^{Cr}$)
$GdCrO_3$	F_xC_y	F_xG_z	√	G_xF_z
$TbCrO_3$	F_xC_y	–	–	F_xG_z
$DyCrO_3$	G_xA_y	–	–	F_xG_z
$HoCrO_3$	$-F_x-C_y$	–	–	G_z
$ErCrO_3$	$-C_z$	G_y	√	G_xF_z
$TmCrO_3$	–	–	–	F_xG_z
$YbCrO_3$	–	–	–	F_xG_z
$LuCrO_3$	–	–	–	F_xG_z

The crystal structure is orthorhombic with the *Pbnm* space group (No. 62). Here T_N^{RE} = AFM transition temperature of RE^{3+} ions; SR = spin reorientation; T_{SR}^{Cr} = SR temperature of Cr^{3+} ions; T_N^{Cr} = AFM transitions temperature of Cr^{3+} ions. The check mark (√) represents that there exists a magnetic SR phase transition. These were summarized from the following references: $GdCrO_3$ (Cooke et al., 1974), $TbCrO_3$ (Gordon et al., 1976), $DyCrO_3$ (Bertaut, 1963; Krynetskii and Matveev, 1997; Tamaki et al., 1975), $HoCrO_3$ (Shamir et al., 1981; Su et al., 2011), $ErCrO_3$ (Hornreich, 1978; Shamir et al., 1981), $TmCrO_3$ (Shamir et al., 1981), $YbCrO_3$ (Shamir et al., 1981), and $LuCrO_3$ (Shamir et al., 1981).

of 1.5–120 K (Deepak et al., 2021). Unraveling the nature of the magnetic phase transitions necessitates neutron scattering studies on single-crystal samples with modern techniques (Li, 2008).

DISCUSSION

Superexchange interactions between the neighboring spins of transition metals can be realized through VCT via intermediate O^{2-} ions. During this process, the tilting of the oxygen octahedron corresponds to the change in the metal-oxygen-metal bond angles and may lead to t_{2g} and e_g orbital overlapping. This facilitates the hopping of $t_{2g\uparrow}$ electrons via the bridge of O^{2-} ions to occupy the empty e_g band and the interaction with filled $t_{2g\downarrow}$ electrons at the same site, that is, the intersite t-e orbital hybridization (Zhou et al., 2010; Zhou and Goodenough, 2008). In the framework of t-e hybridization, the superexchange parameter J consists of the following two parts (Zhou et al., 2010):

$$J = J^\pi - J_{hb}^\sigma, \qquad (\text{Equation 2})$$

where J^π denotes AFM coupling via the VCT of $t_{2g}^3 - O - t_{2g}^3$, and J_{hb}^σ represents FM coupling via the VCT of $t_{2g}^3 - O - e_g^2$. Both processes are schematically depicted in Figure 11A for Cr^{3+} ions. For example, for a half-filled transition metal like Fe^{3+} ($t_{2g}^3 e_g^2$), the effect of t-e hybridization on superexchange interactions may not be evident because the electron hoppings of $Fe^{3+}(t_{2g\uparrow}^3) - O^{2-} Fe^{3+}(t_{2g\downarrow}^3)$ and $Fe^{3+}(t_{2g\uparrow}^3) - O^{2-} - Fe^{3+}(e_{g\downarrow}^2)$ themselves are AFM couplings already (Zhou et al., 2010; Zhou and Goodenough, 2008). In contrast, for less than half-filled $3d$ electrons like Cr^{3+} ions ($t_{2g}^3 e_g^0$) in $RECrO_3$ compounds, the t-e orbital hybridization favors the VCT of $Cr^{3+}(t_{2g\uparrow}^3) - O^{2-} - Cr^{3+}(e_g^0)$ (Qian et al., 2014; Siddique et al., 2021; Zhou et al., 2010). Electron hopping of $t_{2g}^3 - O - e_g^0$ can increase the FM coupling component J_{hb}^σ. When RE^{3+} ions change from La to Lu in $RECrO_3$, the competition between the AFM (J^π) and FM (J_{hb}^σ) components would probably result in a variation in T_N^{Cr}.

To quantitatively describe the Cr^{3+}-O^{2-}-Cr^{3+} superexchange interactions as well as the $t_{2g} - e_g$ (t-e) orbital overlapping degree as a function of the ionic radii of the RE^{3+} ions, we calculated the exchange parameters and electronic structures of $RECrO_3$ (RE = Y, Eu, Gd, Tb, Dy, Ho, Er, Tm, Yb, and Lu) compounds. We mainly considered the NN exchange parameters of the Cr^{3+} sublattices within the crystallographic ab plane (J_1) and along the c axis (J_2) (Figure 11B). We extracted the values of J_1 and J_2 using the so-called energy mapping method with four types of magnetic structures (A-AFM, C-AFM, G-AFM, and FM) (Figure S3). We obtained the total energy of each magnetic structure using DFT calculations, projecting each collinear spin state onto the following spin Hamiltonian of a Heisenberg model
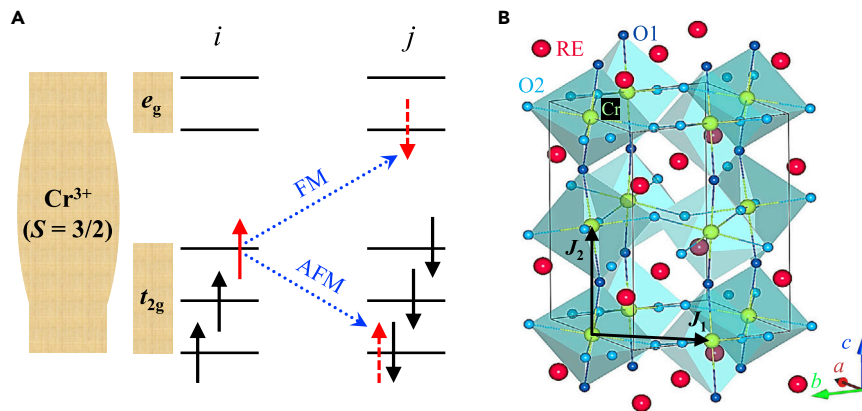
Figure 11. Process of virtual charge transfer and crystal structure

(A) Crystal field splitting of the 5-fold degenerate d orbitals of Cr^{3+} ions ($3d^3$) in a cubic environment that splits the d-level into 2-fold degenerate e_g and 3-fold degenerate t_{2g} levels. The arrows represent the spins of chromium. We schematically show the virtual charge transfers, leading to FM and AFM states, respectively.

(B) Refined crystal structure of $RECrO_3$ in one unit cell (solid lines) with $Pbnm$ space group (No. 62). The RE, Cr, O1, and O2 ions are labeled. J_1 and J_2 represent the NN spin-exchange parameters within the ab plane and along the c axis, respectively.

$$H = -\sum J_{ij} S_i \cdot S_j, \qquad \text{(Equation 3)}$$

where $J > 0$ represents FM interactions, and $J < 0$ denotes AFM couplings. Using Equation (3), we can solve for J_1 and J_2 as (Bernal et al., 2021; Fujioka et al., 2008)

$$J_1 = (E_G + E_C - E_A - E_F)/8S^2, \text{ and} \qquad \text{(Equation 4)}$$

$$J_2 = (E_G - E_C + E_A - E_F)/4S^2. \qquad \text{(Equation 5)}$$

Thus, we can calculate the Néel temperatures of the $RECrO_3$ compounds using the mean-field approximation (MFA) (Fujioka et al., 2008), that is,

$$T_N = \frac{2S(S+1)}{3k_B}(-4J_1 - 2J_2). \qquad \text{(Equation 6)}$$

To depict the hybridization degree, we calculated the overlap of $t_{2g\downarrow}$ and $e_{g\uparrow}$ (Table 3) using their DOS (Figure S4) product over the corresponding energy region.

$$I_{t_{2g\downarrow}-e_{g\uparrow}} = \int_{E_F}^{E_c} D_{t_{2g\downarrow}}(E) D_{e_g\uparrow}(E) dE, \qquad \text{(Equation 7)}$$

where $D_{t_{2g\downarrow}}(E)$ and $D_{e_g\uparrow}(E)$ are the DOSs for the $t_{2g\downarrow}$ and unoccupied $e_{g\uparrow}$ states of Cr^{3+} ions, respectively. E_F and E_c represent the Fermi level and cutoff energy of the $t_{2g\downarrow} - e_{g\uparrow}$ hybridization, respectively. With Equation (7), we could quantitatively describe the t-e hybridization in $RECrO_3$ orthochromates (Table 3).

To illustrate the effect of on-site Coulomb interactions of Cr^{3+} ions on the superexchanges in rare-earth orthochromates, we chose $YbCrO_3$ as an example and carried out a calculation of U_{eff} scan from 0 to 5 eV as shown in Figure 12A, where we can see the U_{eff}-dependent evolution of t-e orbital hybridizations from the DOSs. Based on these calculations, the U_{eff}-dependent exchange parameters of J_1 and J_2 were extracted and shown in Figure 12B. The increase in on-site Coulomb interactions enhances both the crystalline-field splitting and the exchange splitting (with a relatively larger enhancement). The overall superexchange interactions could be expressed as (Zhou et al., 2010)

$$J = J_0\left[(b^\pi)^2 - \eta\left(b_{hb}^\sigma\right)^2\right], \text{ and} \qquad \text{(Equation 8)}$$

$$\eta \propto \frac{U + \Delta_{ex}}{U + \Delta_c}, \qquad \text{(Equation 9)}$$

Table 3. Calculated nearest-neighbor (NN) exchange parameters J_1 and J_2, as well as the ratio J_2/J_1, Néel temperature (T_N^{MFA}) based on the mean-field approximation, t-e orbital overlapping degree ($I_{t_{2g}-e_g}$), and the ordered effective moment ($M_{Cr^{3+}}$) of Cr^{3+} ions in $RECrO_3$ orthochromates

Parameter (unit)	J_1 (meV)	J_2 (meV)	J_2/J_1	T_N^{MFA} (K)	$I_{t_{2g\downarrow}-e_{g\uparrow}}$ (states^2/eV)	$M_{Cr^{3+}}$ (μ_B)
$EuCrO_3$	−1.420	−1.390	0.98	245.7	−2.2104	2.933
$GdCrO_3$	−1.330	−1.210	0.91	224.8	−2.2743	2.931
$TbCrO_3$	−1.140	−0.940	0.82	186.5	−2.3571	2.929
$DyCrO_3$	−1.050	−0.760	0.72	165.9	−2.4040	2.928
$YCrO_3$	−0.990	−0.630	0.63	151.0	−2.4387	2.930
$HoCrO_3$	−0.940	−0.430	0.46	134.3	−2.4602	2.928
$ErCrO_3$	−0.850	−0.230	0.27	112.4	−2.5064	2.927
$TmCrO_3$	−0.720	−0.120	0.17	90.2	−2.5396	2.926
$YbCrO_3$	−0.690	−0.001	0.01	80.5	−2.5786	2.925
$LuCrO_3$	−0.760	−0.046	0.06	91.3	−2.5394	2.925

where U denotes the on-site Coulomb interactions, Δ_{ex} and Δ_c are the exchange splitting and the crystalline-field splitting, respectively (Zhou et al., 2010). In the $RECrO_3$ system, different RE^{3+} ions lead to different crystallographic structures of $RECrO_3$. The increase of U_{eff} favors the ferromagnetic component in the entire superexchange interactions, leading to a strong competition between ferromagnetic and antiferromagnetic components, and finally may result in $J_2 > 0$, that is, ferromagnetism would be generated along the crystallographic c axis.

Different U_{eff}-value settings have a relatively minor effect on the t-e hybridization; therefore, our calculations are based on the on-site Coulomb interactions between Cr^{3+} ions using Hubbard $U_{eff} = 3.3$ eV derived under the framework of a linear-response ansatz, which is in good agreement with the measured band gaps (Singh et al., 2018). Meanwhile, the electron dispersions are not largely influenced by fixing U_{eff}, which assures the calculation of reliable t-e orbital hybridizations of $RECrO_3$ orthochromates by considering only the influence of RE^{3+} ions.

Based on the foregoing discussion, we first optimized the structural parameters of $RECrO_3$ orthochromates (Tables S1 and S2) (Kumar et al., 2008). Our calculations also indicate that the G-type AFM is the most stable magnetic structure for all the $RECrO_3$ orthochromates (Figure S3 and Table S3). Subsequently, we extracted the optimized values of J_1, J_2, Néel temperature (T_N^{MFA}), and the $t_{2g} - e_g$ orbital overlapping degree ($I_{t_{2g}-e_g}$) (Table 3).

When RE^{3+} ions varies from Eu to Lu, the changes of the calculated $I_{t_{2g}-e_g}$ (Figure 13A), T_N^{MFA} (Figure 13B), and $\angle Cr$-O1-Cr and $\angle Cr$-O2-Cr (Figure 13C) demonstrated a similar trend, indicating a strong correlation between them and a clear effect of the RE^{3+} radii (Winter, 2021) on the superexchange interactions. The calculated T_N^{MFA} coincided with the experimental T_N^{Cr} values (Table 1, Figure 13B). The average value ($\langle \angle Cr-O-Cr \rangle$) of the $\angle Cr$-O1(2)-Cr bond angles changed from 148.34° ($EuCrO_3$) to 142.81° ($YbCrO_3$) (Tables S1 and S2), leading to the t-e hybridization ($I_{t_{2g}-e_g}$) changing from −2.2104 ($EuCrO_3$) to −2.5786 states^2/eV ($YbCrO_3$) and the corresponding T_N^{MFA} decreased from 245.7 ($EuCrO_3$) to 80.5 K ($YbCrO_3$) (Table 3). Therefore, the decrease in bond angles of $\angle Cr$-O1(2)-Cr facilitated t-e hybridization by enhancing the FM component (J_{hb}^σ) within the entire superexchange interaction. Both our experimental and theoretical studies produced the minimum AFM transition temperature for $YbCrO_3$ in the system (Figure 13B), which is inconsistent with a previous study on polycrystal $RECrO_3$ samples, where the minimum T_N and $\langle \angle Cr - O - Cr \rangle$, occurred to $LuCrO_3$ (Zhou and Goodenough, 2008).

Our DFT calculations demonstrate that the magnetic anisotropy of Cr^{3+} sublattices can be tuned by RE^{3+} ions. The ratio of J_2/J_1 is a good parameter that inversely expresses anisotropy. It indeed reduces from $J_2/J_1 \sim 0.98$ ($EuCrO_3$) to ~ 0.01 ($YbCrO_3$) (Table 3) and strongly correlates with the values of the $\angle Cr$-O1(2)-Cr bond angles. The $\angle Cr$-O1-Cr angle was outside the ab plane, and its value was smaller than that of $\angle Cr$-O2-Cr within the ab plane (Inset, Figure 13C). Therefore, we infer that the VCT of $t_{2g\uparrow}^3 - O^{2-} - t_{2g\downarrow}^3$ produces
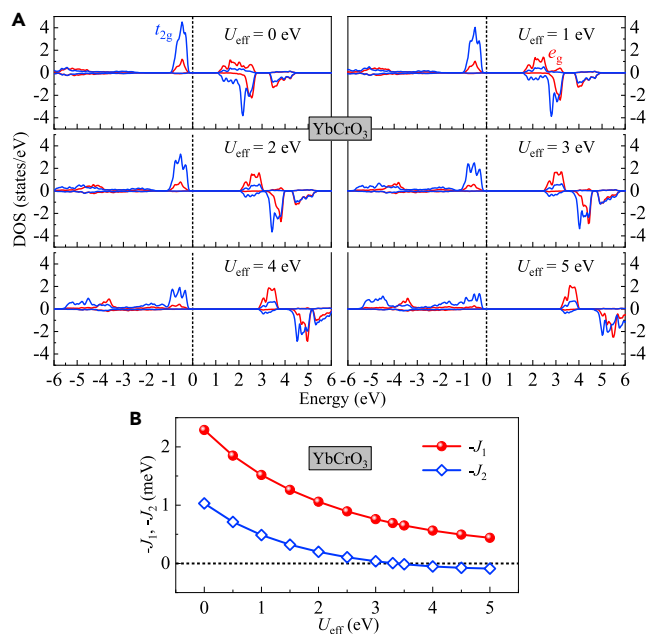
Figure 12. Calculated DOSs, J_1 and J_2 of YbCrO$_3$

(A) Calculated DOSs of t_{2g} and e_g orbitals (as marked) of Cr^{3+} ions in YbCrO$_3$ at U_{eff} = 0, 1, 2, 3, 4, and 5 eV. The positive and negative values represent high-spin and low-spin states, respectively. The vertical short-dotted lines at energy = 0 eV denote the Fermi level.

(B) Calculated exchange parameters J_1 (within the ab plane) and J_2 (along the c axis) as a function of U_{eff} for the YbCrO$_3$ compound. Related to Discussion.

the major AFM spin interactions within the ab plane, whereas the VCT of $t_{2g\uparrow}^3 - O^{2-} - e_g^0$ can generate strong FM couplings along the c axis. This is in good agreement with the previously proposed magnetic model (Van der Ziel and Van Uitert, 1969). The difference between the $\angle$Cr-O1(2)-Cr values increases when RE^{3+} varies from Eu to Lu, indicating that the competition between in-plane AFM interactions and out-of-plane FM couplings becomes increasingly strong with an enhancement of FM interactions. The largest difference between $\angle$Cr-O1-Cr and $\angle$Cr-O2-Cr occurred for YbCrO$_3$, leading to the smallest J_2/J_1 ratio (~0.01), and thus the largest magnetic anisotropy.

The FM coupling J_{hb}^σ directly acts on the overall Cr-O-Cr superexchange. This is induced by the $t_{2g} - t_{2g}$ orbital hybridization and could compete with AFM coupling, leading to an overall exchange $J = J^\pi - J_{hb}^\sigma$ (Zhou et al., 2010). The state of Cr^{3+}, that is, the $3d^3$ configuration with half-filled t_{2g} orbital and empty e_g orbital, makes it a special ion compared with other elements such as V, Fe, and Mn (Streltsov and Khomskii, 2008). By chemical engineering (Yaresko, 2008) or applying high pressure (Fita et al., 2021), one may strengthen $t_{2g} - t_{2g}$ hopping but simultaneously weaken $t_{2g} - t_{2g}$ hopping. Eventually, this could result in an overall FM component superexchange between neighboring Cr^{3+} cations. The weak ferromagnetism results from competition between the Heisenberg exchange and DM interactions in orthochromates. This is one case of an AFM structure with a small canting, leading to a noncollinear spin configuration and thus a net FM component. Unraveling the competing degree of different spin interactions necessitates inelastic neutron scattering studies on single-crystal orthochromates.

Conclusion

We have successfully grown a series of RECrO$_3$ (RE = Y, Eu–Lu) single crystals with a laser-diode FZ furnace. The grown crystals are centimeter (gram)-scale with a good quality. We performed magnetization measurements as functions of temperature and applied magnetic field, providing more reliable and intrinsic magnetic properties. We theoretically investigated the t-e hybridization by quantitatively calculating the t_{2g} and e_g orbital overlapping degree ($I_{t_{2g\downarrow} - e_{g\uparrow}}$) based on DOS calculations. As RE^{3+} ions change from Eu to Lu, the calculated AFM transition temperatures demonstrate a similar trend with those determined experimentally. The changes in the $\angle$Cr-O1(2)-Cr bond angles strongly influence the weight factor of FM couplings

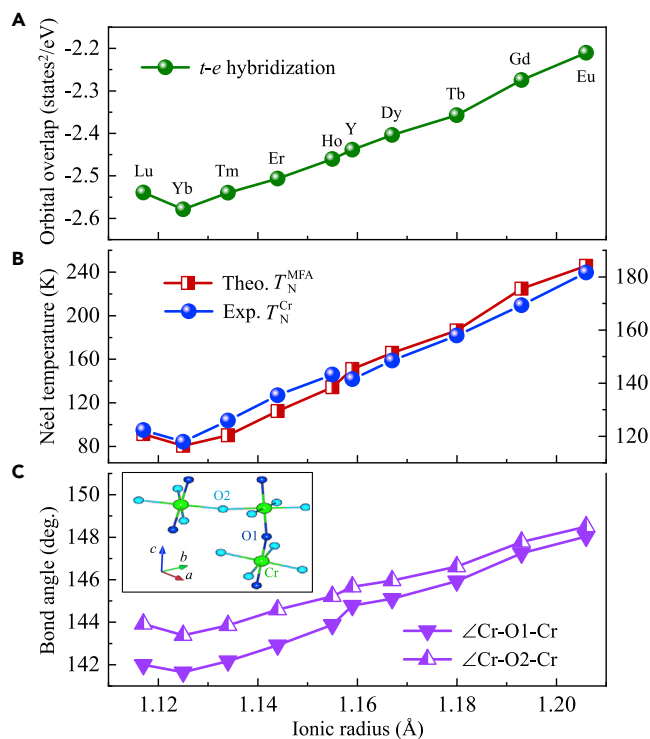**Figure 13. Coincidence between experimental and theoretical properties**

(A) Calculated t-e orbital overlapping degree ($I_{t_{2g\downarrow}-e_{g\uparrow}}$).

(B) Experimental (T_N^{Cr}) (right) and calculated (T_N^{MFA}) (left) AFM transition temperatures.

(C) Theoretically optimized values of $\angle$Cr-O1(O2)-Cr bond angles of RECrO$_3$ (RE = Eu, Gd, Tb, Dy, Y, Ho, Er, Tm, Yb, and Lu) compounds. Inset of (C) shows the geometry of bond angles. The horizontal axis represents ionic radii of RE^{3+} ions.

within the entire superexchanges interactions by (dis)favoring the VCT of $t_{2g\uparrow}^3 - O^{2-} - e_g^0$. This may be the origin of the weak ferromagnetism appearing within the main AFM matrix of RECrO$_3$. The difference between $\angle$Cr-O1(2)-Cr bond angles results in a magnetic anisotropy between within the ab plane and along the c axis. The change of t-e hybridization coincides well with that of $\angle$Cr-O1(2)-Cr and that of T_N^{MFA}. Our research sheds light on the origin of the intriguing magnetism in the RECrO$_3$ system.

Limitations of the study

The single crystal growth of orthochromates is extremely difficult. First, traditional FZ furnaces equipped with four IR-heating halogen lamps and four ellipsoidal mirrors (such as Model FZ-T-10000-H-VI-VPO-PC from Crystal Systems Inc.) cannot even access the melting temperature of orthochromates so that the seed and feed rods could not be melted, thus the crystal growth could not be performed. Second, the evaporation of Cr-based oxides is very heavy like a thick haze. Third, the process of crystal growth is time-consuming and labor-intensive, and one needs to optimize various growth parameters. Presently, we are unable to measure magnetic properties as a function of the crystallographic orientation because of technique difficulties, which is left for future work.

STAR★METHODS

Detailed methods are provided in the online version of this paper and include the following:

- KEY RESOURCES TABLE
- RESOURCE AVAILABILITY
  - Lead contact
  - Materials availability
  - Data and code availability
- METHOD DETAILS

- ○ Single crystal growth procedure and parameters
- ○ Neutron Laue diffraction
- ○ Magnetization measurements
- ○ First-principles calculations
- QUANTIFICATION AND STATISTICAL ANALYSIS

SUPPLEMENTAL INFORMATION

Supplemental information can be found online at https://doi.org/10.1016/j.isci.2022.104111.

AUTHOR CONTRIBUTIONS

Y.H.Z., J.C.X., and S.W. contributed equally.

Y.H.Z., J.C.X., S.W., Y.Z., L.W., H.W., J.H.F., C.Y.W., T.W., Y.S., and J.D.Y. grew the single crystals. Y.H.Z., S.W., Y.Z., L.W., and H.W. performed the Laue experiments. Y.H.Z., J.C.X., S.W., and K.T.S. performed magnetization measurements. Y.H.Z., Y.W.Y., Y.L.Z., H.W.K., and R.Q.Z. carried out the theoretical calculations. All authors discussed and analyzed the results. Y.H.Z. and H.F.L. wrote the main manuscript text. All authors reviewed the paper. R.Q.Z. and H.F.L. conceived and directed the project.

DECLARATION OF INTERESTS

The authors declare the following competing financial interest(s): Y. H. Zhu, S. Wu, and H.-F. Li have a 2021 China Invention Patent (CN110904497B) through University of Macau based on this work: A method of centimeter-sized single crystal growth of chromate compounds and related storage device.

REFERENCES

Bernal, F.L.M., Lundvall, F., Kumar, S., Hansen, P.-A.S., Wragg, D.S., Fjellvåg, H., and Løvvik, O.M. (2021). Jahn-teller active fluoroperovskites $ACrF_3$ (A = Na^+, K^+): magnetic and thermo-optical properties. Phys. Rev. Mater. 5, 064420.

Bertaut, E.F. (1963). Spin Configurations of Ionic Structures: Theory and Practice. In Magnetism iii, 3, G.T. Rado and H. Suhl, eds (Academic Press), pp. 149–209.

Besbes, O., Nikolaev, S., Meskini, N., and Solovyev, I. (2019). Microscopic origin of ferromagnetism in the trihalides $CrCl_3$ and CrI_3. Phys. Rev. B 99, 104432.

Chatterji, T., Demmel, F., Jalarvo, N., Podlesnyak, A., Kumar, C., Xiao, Y., and Brückel, T. (2017). Quasielastic and low-energy inelastic neutron scattering study of $HoCrO_3$ by high resolution time-of-flight neutron spectroscopy. J. Phys. Condens. Matter 29, 475802.

Cheng, H.-M. (2017). Metre-size single-crystal graphene becomes a reality. Sci. Bull. 62, 1039–1040.

Cococcioni, M., and de Gironcoli, S. (2005). Linear response approach to the calculation of the effective interaction parameters in the LDA + U method. Phys. Rev. B 71, 035105.

Coffey, D., Rice, T.M., and Zhang, F.C. (1991). Dzyaloshinskii-Moriya interaction in the cuprates. Phys. Rev. B 44, 10112–10116.

Cooke, A.H., Martin, D.M., and Wells, M.R. (1974). Magnetic interactions in gadolinium orthochromite, $GdCrO_3$. J. Phys. C: Solid State Phys. 7, 3133–3144.

Deepak, Kumar, A., and Yusuf, S.M. (2021). Intertwined magnetization and exchange bias reversals across compensation temperature in $YbCrO_3$ compound. Phys. Rev. Mater. 5, 124402.

Dmitrienko, V.E., Ovchinnikova, E.N., Collins, S.P., Nisbet, G., Beutier, G., Kvashnin, Y.O.,

Mazurenko, V.V., Lichtenstein, A.I., and Katsnelson, M.I. (2014). Measuring the Dzyaloshinskii-Moriya interaction in a weak ferromagnet. Nat. Phys. 10, 202–206.

Dudarev, S.L., Botton, G.A., Savrasov, S.Y., Humphreys, C.J., and Sutton, A.P. (1998). Electron-energy-loss spectra and the structural stability of nickel oxide: an lsda+u study. Phys. Rev. B 57, 1505–1509.

Durán, A., Meza F., C., Morán, E., Alario-Franco, M.A., and Ostos, C. (2014). Biferroic LuCrO$_3$: structural characterization, magnetic and dielectric properties. Mater. Chem. Phys. 143, 1222–1227.

Eibschütz, M., Holmes, L., Maita, J.P., and Van Uitert, L.G. (1970). Low temperature magnetic phase transition in ErCrO$_3$. Solid State Commun. 8, 1815–1817.

El Amrani, M., Zaghrioui, M., Ta Phuoc, V., Gervais, F., and Massa, N.E. (2014). Local symmetry breaking and spin-phonon coupling in SmCrO$_3$ orthochromite. J. Magn. Magn. Mater. 361, 1–6.

Fiebig, M., Lottermoser, T., Meier, D., and Trassin, M. (2016). The evolution of multiferroics. Nat. Rev. Mater. 1, 16046.

Fita, I., Puzniak, R., and Wisniewski, A. (2021). Pressure-tuned spin switching in compensated GdCrO$_3$ ferrimagnet. Phys. Rev. B 103, 054423.

Franchini, C., Podloucky, R., Paier, J., Marsman, M., and Kresse, G. (2007a). Ground-state properties of multivalent manganese oxides: density functional and hybrid density functional calculations. Phys. Rev. B 75, 195128.

Franchini, C., Podloucky, R., Paier, J., Marsman, M., and Kresse, G. (2007b). Ground-state properties of multivalent manganese oxides: density functional and hybrid density functional calculations. Phys. Rev. B 75, 195128.

Fujioka, Y., Frantti, J., and Nieminen, R.M. (2008). Electronic energy band structure of the double perovskite Ba$_2$MnWO$_6$. J. Phys. Chem. B 112, 6742–6746.

Gordon, J.D., Hornreich, R.M., Shtrikman, S., and Wanklyn, B.M. (1976). Magnetization studies in the rare-earth orthochromites. v. TbCrO$_3$ and PrCrO$_3$. Phys. Rev. B 13, 3012–3017.

Hornreich, R.M. (1978). Magnetic interactions and weak ferromagnetism in the rare-earth orthochromites. J. Magn. Magn. Mater. 7, 280–285.

Huang, K.-W., Yi, S.-H., Jiang, Y.-S., Kao, W.-C., Yin, Y.-T., Beck, D., Korolkov, V., Proksch, R., Shieh, J., and Chen, M.-J. (2021). Sub-7-nm textured ZrO$_2$ with giant ferroelectricity. Acta Materialia 205, 116536.

Hur, N., Park, S., Sharma, P.A., Ahn, J.S., Guha, S., and Cheong, S.-W. (2004). Electric polarization reversal and memory in a multiferroic material induced by magnetic fields. Nature 429, 392–395.

Jones, P.P., Gaw, S.M., Doig, K.I., Prabhakaran, D., Hétroy Wheeler, E.M., Boothroyd, A.T., and Lloyd-Hughes, J. (2014). High-temperature electromagnons in the magnetically induced multiferroic cupric oxide driven by intersublattice exchange. Nat. Commun. 5, 3787.

Ko, E., Kim, B.J., Kim, C., and Choi, H.J. (2007). Strong orbital-dependent d-band hybridization and fermi-surface reconstruction in metallic Ca$_{2-x}$Sr$_x$RuO$_4$. Phys. Rev. Lett. 98, 226401.

Kresse, G., and Furthmüller, J. (1996a). Efficiency of ab-initio total energy calculations for metals and semiconductors using a plane-wave basis set. Compt. Mater. Sci. 6, 15–50.

Kresse, G., and Furthmüller, J. (1996b). Efficient iterative schemes for ab initio total-energy calculations using a plane-wave basis set. Phys. Rev. B 54, 11169–11186.

Kresse, G., and Joubert, D. (1999). From ultrasoft pseudopotentials to the projector augmented-wave method. Phys. Rev. B 59, 1758–1775.

Krynetskii, I.B., and Matveev, V.M. (1997). Metamagnetism and magnetostriction of the Ising antiferromagnet DyCrO$_3$. Phys. Solid State 39, 584–585.

Kumar, A., Verma, A., and Bhardwaj, S. (2008). Prediction of formability in perovskite-type oxides. Open Appl. Phys. J. 1, 11–19.

Kumar, C.M.N., Xiao, Y., Nair, H.S., Voigt, J., Schmitz, B., Chatterji, T., Jalarvo, N.H., and Brückel, T. (2016). Hyperfine and crystal field interactions in multiferroic HoCrO$_3$. J. Phys. Condens. Matter 28, 476001.

Landron, S., and Lepetit, M.-B. (2008). Importance of t_{2g}-e_g hybridization in transition metal oxides. Phys. Rev. B 77, 125106.

Li, H.-F. (2008). Synthesis of CMR Manganites and Ordering Phenomena in Complex Transition Metal Oxides (Forschungszentrum Jülich GmbH Press), Ph.D. thesis.

Li, H.-F. (2016). Possible ground states and parallel magnetic-field-driven phase transitions of collinear antiferromagnets. Npj Comput. Mater. 2, 1–8.

Li, H., Su, Y., Persson, J., Meuffels, P., Walter, J., Skowronek, R., and Brückel, T. (2006). Correlation between structural and magnetic properties of La$_{7/8}$Sr$_{1/8}$Mn$_{1-\gamma}$O$_{3+\delta}$ with controlled nonstoichiometry. J. Phys. Condens. Matter 19, 016003.

Li, H., Su, Y., Persson, J., Meuffels, P., Walter, J., Skowronek, R., and Brückel, T. (2007). Neutron-diffraction study of structural transition and magnetic order in orthorhombic and rhombohedral La$_{7/8}$Sr$_{1/8}$Mn$_{1-\gamma}$O$_{3+\delta}$. J. Phys. Condens. Matter 19, 176226.

Li, H.-F., Su, Y., Xiao, Y., Persson, J., Meuffels, P., and Brückel, T. (2009). Crystal and magnetic structure of single-crystal La$_{1-x}$Sr$_x$MnO$_3$ ($x \approx 1/8$). Eur. Phys. J. B 67, 149–157.

Li, Y.-T., Gou, G.-Y., Li, L.-S., Tian, H., Cong, X., Ju, Z.-Y., Tian, Y., Geng, X.-S., Tan, P.-H., Yang, Y., et al. (2018). Millimeter-scale nonlocal photo-sensing based on single-crystal perovskite photodetector. IScience 7, 110–119.

Li, H., Zhu, Y., Wu, S., and Tang, Z. (2021). A Method of Centimeter-Sized Single Crystal Growth of Chromate Compounds and Related Storage Device, China Patent CN110904497B.

Looby, J.T., and Katz, L. (1954). Yttrium chromium oxide, a new compound of the perowskite type. J. Am. Chem. Soc. 76, 6029–6030.

Monkhorst, H.J., and Pack, J.D. (1976). Special points for brillouin-zone integrations. Phys. Rev. B 13, 5188–5192.

Oliveira, G. (2017). Local Probing Spinel and Perovskite Complex Magnetic Systems (Universidade do Porto), Ph.D. thesis.

Oliveira, G.N.P., Teixeira, R.C., Moreira, R.P., Correia, J.G., Araújo, J.P., and Lopes, A.M.L. (2020). Local inhomogeneous state in multiferroic SmCrO$_3$. Sci. Rep. 10, 4686.

Ouladdiaf, B., Archer, J., McIntyre, G.J., Hewat, A.W., Brau, D., and York, S. (2006). Orientexpress: a new system for laue neutron diffraction. Physica B Condens. Matter 385, 1052–1054.

Perdew, J.P., Burke, K., and Ernzerhof, M. (1996). Generalized gradient approximation made simple. Phys. Rev. Lett. 77, 3865–3868.

Philipp, J.B., Majewski, P., Alff, L., Erb, A., Gross, R., Graf, T., Brandt, M.S., Simon, J., Walther, T., Mader, W., et al. (2003). Structural and doping effects in the half-metallic double perovskite A$_2$CrWO$_6$ (A = Sr, Ba, and Ca). Phys. Rev. B 68, 144431.

Preethi Meher, K.R.S., Wahl, A., Maignan, A., Martin, C., and Lebedev, O.I. (2014). Observation of electric polarization reversal and magnetodielectric effect in orthochromites: a comparison between LuCrO$_3$ and ErCrO$_3$. Phys. Rev. B 89, 144401.

Qian, X., Chen, L., Cao, S., and Zhang, J. (2014). A study of the spin reorientation with t–e orbital hybridization in SmCrO$_3$. Solid State Commun. 195, 21–25.

Rajeswaran, B., Khomskii, D.I., Zvezdin, A.K., Rao, C.N.R., and Sundaresan, A. (2012). Field-induced polar order at the Néel temperature of chromium in rare-earth orthochromites: interplay of rare-earth and Cr magnetism. Phys. Rev. B 86, 214409.

Serrao, C.R., Kundu, A.K., Krupanidhi, S.B., Waghmare, U.V., and Rao, C.N.R. (2005). Biferroic YCrO$_3$. Phys. Rev. B 72, 220101.

Shamir, N., Shaked, H., and Shtrikman, S. (1981). Magnetic structure of some rare-earth orthochromites. Phys. Rev. B 24, 6642–6651.

Shi, J., Yin, S., Seehra, M.S., and Jain, M. (2018). Enhancement in magnetocaloric properties of ErCrO$_3$ via A-site Gd substitution. J. Appl. Phys. 123, 193901.

Shick, A.B., Liechtenstein, A.I., and Pickett, W.E. (1999). Implementation of the LDA+U method using the full-potential linearized augmented plane-wave basis. Phys. Rev. B 60, 10763–10769.

Siddique, M.N., Faizan, M., Riyajuddin, S., Tripathi, P., Ahmad, S., and Ghosh, K. (2021). Intrinsic structural distortion assisted optical and magnetic properties of orthorhombic rare-earth perovskite La$_{1-x}$Eu$_x$CrO$_3$: effect of te hybridization. J. Alloys Compd. 850, 156748.

Singh, K.D., Pandit, R., and Kumar, R. (2018). Effect of rare earth ions on structural and optical properties of specific perovskite orthochromates;

RCrO$_3$ (R = La, Nd, Eu, Gd, Dy, and Y). Solid State Sci. *85*, 70–75.

Slater, J.C., and Koster, G.F. (1954). Simplified LCAO method for the periodic potential problem. Phys. Rev. *94*, 1498–1524.

Spaldin, N.A., and Ramesh, R. (2019). Advances in magnetoelectric multiferroics. Nat. Mater. *18*, 203–212.

Streltsov, S.V., and Khomskii, D.I. (2008). Electronic structure and magnetic properties of pyroxenes (Li,Na)TM(Si,Ge)$_2$O$_6$: low-dimensional magnets with 90°bonds. Phys. Rev. B *77*, 064405.

Su, Y., Zhang, J., Feng, Z., Li, L., Li, B., Zhou, Y., Chen, Z., and Cao, S. (2010a). Magnetization reversal and Yb^{3+}/Cr^{3+} spin ordering at low temperature for perovskite YbCrO$_3$ chromites. J. Appl. Phys. *108*, 013905.

Su, Y., Zhang, J., Li, L., Li, B., Zhou, Y., Deng, D., Chen, Z., and Cao, S. (2010b). Temperature dependence of magnetic properties and change of specific heat in perovskite ErCrO$_3$ chromites. Appl. Phys. A. *100*, 73–78.

Su, Y., Zhang, J., Feng, Z., Li, Z., Yan, S., and Cao, S. (2011). Magnetic properties of rare earth HoCrO$_3$ chromites. J. Rare Earth. *29*, 1060–1065.

Su, Y., Zhang, J., Li, B., Kang, B., Yu, Q., Jing, C., and Cao, S. (2012). The dependence of magnetic properties on temperature for rare earth ErCrO$_3$ chromites. Ceram. Int. *38*, S421–S424.

Sun, D., Deng, G.-H., Xu, B., Xu, E., Li, X., Wu, Y., Qian, Y., Zhong, Y., Nuckolls, C., Harutyunyan, A.R., et al. (2019). Anisotropic singlet fission in single crystalline hexacene. iScience *19*, 1079–1089.

Taheri, M., Razavi, F.S., Yamani, Z., Flacau, R., Reuvekamp, P.G., Schulz, A., and Kremer, R.K. (2016). Magnetic structure, magnetoelastic coupling, and thermal properties of EuCrO$_3$ nanopowders. Phys. Rev. B *93*, 104414.

Tamaki, T., Tsushima, K., and Yamaguchi, Y. (1975). Magnetization process in DyCrO$_3$. AIP Conf. Proc. *24*, 69–70.

Tamaki, T., Tsushima, K., and Yamaguchi, Y. (1977). Spin reorientation in TmCrO$_3$. Physica B+C *86*, 923–924.

Vagadia, M., Rayaprol, S., and Nigam, A. (2018). Influence of mn-substitution on the magnetic and thermal properties of TbCrO$_3$. J. Alloys Compd. *735*, 1031–1040.

Wang, L., Rao, G.H., Zhang, X., Zhang, L.L., Wang, S.W., and Yao, Q.R. (2016a). Reversals of magnetization and exchange-bias in perovskite chromite TmCrO$_3$. Ceram. Int. *42*, 10171–10174.

Wang, L., Wang, S.W., Zhang, X., Zhang, L.L., Yao, R., and Rao, G.H. (2016b). Reversals of magnetization and exchange-bias in perovskite chromite YbCrO$_3$. J. Alloys Compd. *662*, 268–271.

Winter, M. (2021). Source: Webelements. http://www.webelements.com/.

Wu, S., Zhu, Y., Gao, H., Xiao, Y., Xia, J., Zhou, P., Ouyang, D., Li, Z., Chen, Z., Tang, Z., et al. (2020). Super-necking crystal growth and structural and magnetic properties of SrTb$_2$O$_4$ single crystals. ACS omega *5*, 16584–16594.

Xiong, P., Peng, M., and Yang, Z. (2021). Near-infrared mechanoluminescence crystals: a review. iScience *24*, 101944.

Yaresko, A.N. (2008). Electronic band structure and exchange coupling constants in ACr$_2$X$_4$ spinels (A = Zn, Cd, Hg; X = O, S, Se). Phys. Rev. B *77*, 115106.

Yekta, Y., Hadipour, H., Şaşıoğlu, E., Friedrich, C., Jafari, S.A., Blügel, S., and Mertig, I. (2021). Strength of effective Coulomb interaction in two-dimensional transition-metal halides MX$_2$ and MX$_3$ (M = Ti, V, Cr, Mn, Fe, Co, Ni; X = Cl, Br, I). Phys. Rev. Mater. *5*, 034001.

Yin, L., Yang, J., Tong, P., Luo, X., Park, C., Shin, K., Song, W., Dai, J., Kim, K., Zhu, X., et al. (2016). Role of rare earth ions in the magnetic, magnetocaloric and magnetoelectric properties of RCrO$_3$ (R = Dy, Nd, Tb, Er) crystals. J. Mater. Chem. C *4*, 11198–11204.

Yin, L.H., Shi, T.F., Zhang, R.R., Park, C.B., Kim, K.H., Yang, J., Tong, P., Song, W.H., Dai, J.M., Zhu, X.B., et al. (2018). Electric dipoles via Cr^{3+}(d^3)

ion off-center displacement in perovskite DyCrO$_3$. Phys. Rev. B *98*, 054301.

Yin, L.H., Yang, J., Kan, X.C., Song, W.H., Dai, J.M., and Sun, Y.P. (2015). Giant magnetocaloric effect and temperature induced magnetization jump in GdCrO$_3$ single crystal. J. Appl. Phys. *117*, 133901.

Yoshii, K. (2012). Magnetization reversal in TmCrO$_3$. Mater. Res. Bull. *47*, 3243–3248.

Yoshii, K., and Ikeda, N. (2019). Dielectric and magnetocaloric study of TmCrO$_3$. J. Alloys Compd. *804*, 364–369.

Zhang, Y. (2020). Building a library of metre-scale high-index single-crystal copper foils. Sci. Bull. *65*, 1694–1695.

Zhou, J.-S., Alonso, J.A., Pomjakushin, V., Goodenough, J.B., Ren, Y., Yan, J.-Q., and Cheng, J.-G. (2010). Intrinsic structural distortion and superexchange interaction in the orthorhombic rare-earth perovskites RCrO$_3$. Phys. Rev. B *81*, 214115.

Zhou, J.-S., and Goodenough, J.B. (2008). Intrinsic structural distortion in orthorhombic perovskite oxides. Phys. Rev. B *77*, 132104.

Zhu, Y., Fu, Y., Tu, B., Li, T., Miao, J., Zhao, Q., Wu, S., Xia, J., Zhou, P., Huq, A., et al. (2020a). Crystalline and magnetic structures, magnetization, heat capacity, and anisotropic magnetostriction effect in a yttrium-chromium oxide. Phys. Rev. Mater. *4*, 094409.

Zhu, Y., Wu, S., Tu, B., Jin, S., Huq, A., Persson, J., Gao, H., Ouyang, D., He, Z., Yao, D.-X., et al. (2020b). High-temperature magnetism and crystallography of a YCrO$_3$ single crystal. Phys. Rev. B *101*, 014114.

Zhu, Y., Zhou, P., Li, T., Xia, J., Wu, S., Fu, Y., Sun, K., Zhao, Q., Li, Z., Tang, Z., et al. (2020c). Enhanced magnetocaloric effect and magnetic phase diagrams of single-crystal GdCrO$_3$. Phys. Rev. B *102*, 144425.

Van der Ziel, J.P., and Van Uitert, L.G. (1969). Magnon-assisted optical emission in YCrO$_3$ and LuCrO$_3$. Phys. Rev. *179*, 343–351.

STAR★METHODS

KEY RESOURCES TABLE

REAGENT or RESOURCE	SOURCE	IDENTIFIER
Chemicals, Peptides, and Recombinant Proteins		
Yttrium(III) oxide	Alfa Aesar	CAS: 1314-36-9
Gadolinium(III) oxide	Alfa Aesar	CAS: 12064-62-9
Terbium(III, IV) oxide	Alfa Aesar	CAS: 12037-01-3
Dysprosium(III) oxide	Alfa Aesar	CAS: 1308-87-8
Holmium(III) oxide	Alfa Aesar	CAS: 12055-62-8
Erbium(III) oxide	Alfa Aesar	CAS: 12061-16-4
Thulium(III) oxide	Alfa Aesar	CAS: 12036-44-1
Ytterbium(III) oxide	Alfa Aesar	CAS: 1314-37-0
Lutetium(III) oxide	Alfa Aesar	CAS: 12032-20-1
Chromium(III) oxide	Alfa Aesar	CAS: 1308-38-9
Software and Algorithms		
Origin2016	OriginLab Corporation	https://www.originlab.com/
OrientExpress	(Ouladdiaf et al., 2006)	https://neutronoptics.com/OrientExpress.html
VASP 5.4.4	(Kresse and Furthmüller, 1996a, 1996b)	https://www.vasp.at/

RESOURCE AVAILABILITY

Lead contact

Further information and requests for resources should be directed to and will be fulfilled by the lead contact, Prof. Dr. Hai-Feng Li (haifengli@um.edu.mo).

Materials availability

This long-term project produced a series of $RECrO_3$ (RE = Y, Eu, Gd, Tb, Dy, Ho, Er, Tm, Yb, and Lu) single crystals utilizing the innovative method described in the China Invention Patent (CN110904497B). We welcome potential collaborations.

Data and code availability

- All data reported in this article will be shared by the lead contact upon request.

- Code with instructions reported in this article will be shared by the lead contact upon request.

- Any additional information required to reanalyse the data reported in this study is available from the lead contact upon request.

METHOD DETAILS

Single crystal growth procedure and parameters

Using raw materials of Y_2O_3 (Alfa Aesar, 99.9%), Gd_2O_3 (Alfa Aesar, 99.9%), Tb_4O_7 (Alfa Aesar, 99.9%), Dy_2O_3 (Alfa Aesar, 99.9%), Ho_2O_3 (Alfa Aesar, 99.9%), Er_2O_3 (Alfa Aesar, 99.9%), Tm_2O_3 (Alfa Aesar, 99.9%), Yb_2O_3 (Alfa Aesar, 99.9%), Lu_2O_3 (Alfa Aesar, 99.9%), and Cr_2O_3 (Alfa Aesar, 99.6%), polycrystalline $RECrO_3$ samples were synthesized with solid-state reactions. We first obtained homogeneous polycrystalline powder with a single phase. After that, cylindrical feed rods with additional treatments (Li et al., 2021) were shaped by a hydrostatic pressure of ~70 MPa (Wu et al., 2020; Zhu et al., 2020b). Then $RECrO_3$ single crystals were grown by a laser-diode floating-zone furnace (Model: LD-FZ-5-200W-VPO-PCUM). The floating-zone method assures no introduction of impurities (Li, 2008). The growth speed was fixed at 5–15 mm/h to attain a stable growth state. Due to the intense volatility of chromium oxides, we added extra

5–15% mole raw chromium oxide for the synthesis of polycrystalline samples and for the growth of single crystals.

Neutron Laue diffraction

To determine the quality of the grown single crystals, we performed a neutron Laue diffraction study on the diffractometer, OrientExpress, located at ILL, Grenoble, France. Simultaneously, we simulated the recorded neutron Laue patterns along the three crystallograhpic axes with the software of OrientExpress (Ouladdiaf et al., 2006) to confirm the quality of the grown crystals.

Magnetization measurements

Magnetization was measured using the option of a vibrating sample magnetometer of Quantum Design physical property measurement system. Small $RECrO_3$ single crystals (5–15 mg) were glued on a quartz sample holder with GE Varnish. The dc magnetization was measured at applied magnetic fields of 0, 50, and 100 Oe with zero-field cooling and field cooling modes in the temperature range of 1.8–400 K. The magnetic field dependent hysteresis loops were measured from −14 to 14 T at different temperatures within 1.8–300 K.

First-principles calculations

The first-principles calculations of $RECrO_3$ compounds were carried out within density functional theory. The exchange and correlation term in Kohn-Sham equation was treated with the Perdew-Burke-Ernzerhof (PBE) and (PBE + U) functionals (Perdew et al., 1996; Franchini et al., 2007a, 2007b; Shick et al., 1999) using the Vienna Ab-initio Simulation Package (Kresse and Furthmüller, 1996a, 1996b). The core electrons were frozen, and the projected-augmented-wave method was used (Kresse and Joubert, 1999). The Cr $3d4s$, RE (RE = Eu–Lu) elements $5p5d6s$, Y ($4s4p5s4d$), and O $2s2p$ electrons were treated as valence electrons. It is well known that the $4f$ orbitals are tightly localized in comparison to the d orbitals. In the present study, we aim mainly to unravel the effect of lattice variation on Cr^{3+}-O^{2-}-Cr^{3+} superexchange interactions, and the energy scale of RE^{3+}-RE^{3+} exchange interactions is about two magnitudes smaller than that of Cr^{3+}-Cr^{3+}, hence the $4f$ electrons of lanthanide ions could be frozen reasonably. A Gaussian broadening of 0.05 eV was chosen. The set of plane-wave basis with an energy cutoff of 500 eV was used. Brillouin-zone integrations were performed with a Gamma-point-centered 7 × 7 × 5 Monkhorst-Pack k-point mesh (Monkhorst and Pack, 1976). The ionic relaxation was performed with a convergency criterion of 10^{-5} eV/primitive cell for each relaxation step and stopped moving when residual force <0.01 eV/Å. A convergence accuracy of 10^{-6} eV per conventional cell was chosen for subsequent static self-consistent calculations.

We first optimized the structures with collinear magnetic configurations of FM and A-type, C-type, and G-type AFM, to determine the magnetic ground state of each compound. Furthermore, to avoid an underestimation of the band gap, the Hubbard U value ($U_{eff} = U - J$) of each compound was calculated using the linear response ansatz (Dudarev et al., 1998; Cococcioni and de Gironcoli, 2005). With appropriate Hubbard U value, static electronic self-consistent calculations were performed using the (PBE + U) method to obtain the exact total energy of the four magnetic states. The exchange parameters, J_i, under classical Heisenberg model could be deduced with the energy mapping method, as does T_N^{Cr} based on the mean-field approximation (MFA). Finally, the electronic structures of the $RECrO_3$ compounds were calculated with reading the charge density of ground state of the magnetic configuration.

QUANTIFICATION AND STATISTICAL ANALYSIS

Sensitivity analysis (one-at-a-time) was carried out to see the effects of parameters in the numerical model.